Part and supports optimization in metal powder bed additive manufacturing using simplified process simulation

Martin Bihr, Grégoire Allaire, Xavier Betbeder-Lauque, Beniamin Bogosel, Felipe Bordeu, Julie Querois

▶ To cite this version:

Part and supports optimization in metal powder bed additive manufacturing using simplified process simulation

Martin Bihr
Safran Tech, Magny-les-Hameaux, France
martin.bihr1@gmail.com

Grégoire Allaire
CMAP, Ecole Polytechnique
Institut Polytechnique de Paris
91128 Palaiseau, France
gregoire.allaire@polytechnique.fr

Xavier Betbeder-Lauque
Safran Additive Manufacturing Campus, Le Haillan, France
xavier.betbeder-lauque@safrangroup.com

Beniamin Bogosel
CMAP, Ecole Polytechnique
Institut Polytechnique de Paris
91128 Palaiseau, France
beniamin.bogosel@polytechnique.edu

Felipe Bordeu
Safran Tech, Magny-les-Hameaux, France
felipe.bordeu@safrangroup.com

Julie Querois
Safran Tech, Magny-les-Hameaux, France
julie.querois@safrangroup.com

December 21, 2021

Abstract

This paper is concerned with shape and topology optimization of parts and their supports, taking into account constraints coming from the metal powder bed additive manufacturing process. Despite the high complexity of this process, it is represented by the simple inherent strain model, which has the advantage of being computationally cheap. Three optimization criteria, evaluated with this model, are proposed to minimize defects caused by additive manufacturing: vertical displacements, residual stresses and deflection of the part after baseplate separation. Combining these criteria with a constraint on the compliance for the final use of the part leads to optimization problems which deliver optimized manufacturable shapes with only a slight loss on the final use performance. The numerical results are assessed by manufacturing some optimized and reference geometries. These experimental results are also used to calibrate the inherent strain model by an inverse analysis. The same type of optimization is applied to supports in the case of a fixed non-optimizable part. For our 3-d numerical tests we rely on the level set method, the notion of shape derivatives and an augmented Lagrangian algorithm for optimization.

1   Introduction

Additive manufacturing (AM) processes raised a lot of interest in the past couple of years due to their ability to built complex parts. In particular metal powder bed additive manufacturing processes avoid many constraints associated to classical manufacturing techniques (casting, milling,...) and use only the right amount of material in order to build the part. More specifically, the most common process used nowadays is *Selective Laser Melting* (SLM), where a laser melts locally a metallic powder bed before another layer is spread after solidification (this process is also called LBM for *Laser Beam Melting*). Even if this layer by layer process offers the possibility to manufacture complex parts [9, 18, 20, 23, 30], it has its own manufacturing constraints. High temperature gradients generated by the laser at each layer induce dilation or local shrinking during the manufacturing, resulting in important deformations at the end of the process as these phenomena are repeated at each layer. A solution is to add extra material, so-called support structures, connecting the part to the baseplate in order to maintain those deformed areas. However, these supports need to be removed at the end of the manufacturing process and it can be a very hard task if they are not easily accessible, not to mention the waste of material used to manufacture them.

Another solution is to modify the geometry of the part itself thanks to shape and topology optimization [1], [10] taking into account these manufacturing constraints on top of the final use performance. This approach has already been pursued in the AM context to reduce so-called overhang regions, most often using a geometric approach [4], [21], [35]. These simple criteria are computationally cheap and often provide meaningful designs. However, in more involved cases it is necessary to rely on a more complex model, modeling the layer-by-layer building process as in [3], [4], [5]. One further advantage of using a layer-by-layer model is that thermo-mechanical effects can be incorporated, at least from a macroscopic point of view, as in [2], [3], [7], [22], [36]. However, even if it is a simplified macroscopic thermo-mechanical model, its numerical simulation is still time consuming, especially in an optimization loop. Therefore, there is a need for a more efficient simulation model for the additive manufacturing process.

In this paper, we propose to work with the so-called *inherent strain* model, which is described in Section 2. It is a purely mechanical model without a thermal equation, which is able to capture the occurrence of manufacturing defects like deformations and residual stresses. This model involves as a source term an inherent strain which is calibrated with experimental data. Section 3 introduces an optimization problem which features two state equation: the linearized elasticity equations for the final use performance of the part, and the inherent strain model for the manufacturing process. The goal of this optimization problem is to reduce the manufacturing defects without degrading too much the final use performance of the part. To compute derivatives for the objective function and constraints the adjoint method is used. One further advantage of the inherent strain model is that, although it is a layer-by-layer process, there is no dependency from one layer to the next one, which implies that its adjoint problem is as simple, without any backward effect as in time evolution problems. These adjoint problems allow us to compute shape derivatives in the framework of the Hadamard method of shape sensitivity. Section 4 is a brief summary of our numerical framework. For shape and topology optimization we rely on the level set method [6]. The mechanical analysis as well as the process simulation are computed with the finite element software FreeFEM++ [19]. The constrained optimization problems are solved with an Augmented Lagrangian algorithm [28].

Section 5 deals with two numerical test cases for optimizing the part only (without supports). Both tests feature a MBB beam: the first case minimizes the vertical displacement during the building process, while the second cases minimizes the thermal residual stresses. These two criteria are computed in terms of the solution of the inherent strain model. A constraint on the final-use compliance is enforced during their minimization. Section 6 investigates a different problem of residual deflection after baseplate separation. The mechanical model is more involved but the optimization framework is the same. Here, the post-manufacturing deflection is minimized with a constraint on the final-use compliance. On purpose, it is applied to the design of an arch, for which the deformation is large enough so it can be easily measured experimentally. Therefore, our numerical results can be assessed by manufacturing several copies of the optimized designs. Section 7 presents the experimental set-up, gives the deflection measures and introduces an inverse analysis which allows us to calibrate the value of the inherent strain tensor. Furthermore, it confirms that our optimized designs have a better performance than the reference designs.

Finally, Section 8 is devoted to the optimization of the supports, the part being fixed. Our optimization approach easily adapts to this classical setting, already studied in [2], [3], [22]. Of course, it could be possible to optimize simultaneously both the part and its supports. We leave it for future work, as well as some further generalizations, which are briefly discussed in the concluding Section 9.

2 A process simulation using the inherent strain method

The inherent strain method was first introduced in [33] and is often used to predict residual stress along a welded joint. This approach has been extended to the SLM process simulation [13], [17], [27], [32] as this technology resembles a layer-by-layer welding process. During this welding, the material is subjected to strong temperature gradients, producing thermal strains. The total strain, denoted by ϵ, is the sum of an elastic contribution ϵ_e (equal to $e(u)$, see below for details) and an inelastic contribution ϵ^*, also called inherent strain (regrouping plastic, thermal and phase transformation contributions, responsible

for the deformation and residual stress formation) leading to the formula

$$\epsilon = \epsilon_e + \epsilon^*. \tag{1}$$

Formula (1) is simple and very convenient to compute the total strain ϵ, since the key ingredient of the inherent strain method is to assume that ϵ^* is known. In SLM many parameters affect the deformation of the part: of course the material properties, but also the machine parameters (power, speed and trajectory of the laser [12], [25], [26], [29]), acting directly on the heating and cooling behaviour of the part that cause the deformation. To find the inherent strain tensor ϵ^* corresponding to a given set of machine parameters, one simple solution is to manufacture a test part, and match the deflection measured experimentally with the one obtained numerically with the right inherent strain tensor. Once this tensor ϵ^* has been obtained by such a calibration process (quite similar to the one presented in Section 7), a reasonably good approximation of the behavior of any part, manufactured with the exact same parameters, can be deduced from the inherent strain model. Of course, the inherent strain model is a simplified representation of the real building process and it is known to have some flaws [14], but for optimization purposes it has the definite advantage of being computationally cheap.

In this paper, we consider a part ω, which is a smooth bounded open set of $\mathbb{R}^n$ (with $n = 2$ or 3 in practice), that has to be manufactured within a build chamber, denoted by D, typically a rectangle. The build direction is vertical and the successive layers are horizontal. The baseplate is modeled by a Dirichlet boundary condition at the bottom side Γ_D, meaning that the part is clamped to the baseplate. All other boundaries, denoted by Γ_N, are traction free. The build chamber D is divided into M macro layers $\mathcal{L}_i$ of equal thickness and intermediate domains D_i, $1 \leq i \leq M$, are defined as the union of the first i layers, so that

$$D_1 \subset ... \subset D_i \subset ... \subset D_M \equiv D.$$

Obviously, $\mathcal{L}_i$ is the last layer of the domain D_i and the characteristic function $\chi_{\mathcal{L}_i}$ of the layer $\mathcal{L}_i$ is defined as

$$\chi_{\mathcal{L}_i}(x) = \begin{cases} 1 & \text{if } x \in \mathcal{L}_i, \\ 0 & \text{if } x \notin \mathcal{L}_i. \end{cases}$$

Apart from Γ_D, the boundary of the intermediate domain D_i is $\Gamma_{N_i} = \partial D_i \setminus \Gamma_D$, which is traction free. A picture of the build chamber D, with the intermediate domains D_i, is shown in Figure 1.

For a given part ω, intermediate shapes ω_i, $1 \leq i \leq M$, are also defined by $\omega_i = \omega \cap D_i$. The traction free boundary of ω_i is defined as $\Gamma_{N_i} = \partial \omega_i \setminus \Gamma_D$. Introducing the Sobolev space of kinematically admissible displacements

$$H^1_{\Gamma_D}(\omega_i) := \left\{ v \in H^1(\omega_i)^n \text{ such that } v = 0 \text{ on } \Gamma_D \right\}, \tag{2}$$

the displacement field u_i is the unique solution in $H^1_{\Gamma_D}(\omega_i)$ of the inherent strain problem

$$\begin{cases} -\text{div}(\sigma_i) & = & 0 & \text{in } \omega_i, \\ \sigma_i & = & A\left(e(u_i) + \epsilon^*_{\mathcal{L}_i}\right) & \text{with } \epsilon^*_{\mathcal{L}_i}(x) = \epsilon^* \chi_{\mathcal{L}_i}(x), \\ \sigma_i n & = & 0 & \text{on } \Gamma_{N_i}, \\ u_i & = & 0 & \text{on } \Gamma_D \cap \partial \omega_i. \end{cases} \tag{3}$$

where ϵ^* is the constant inherent strain and A is the isotropic elasticity tensor, defined for any symmetric matrix ξ by $A\xi = 2\mu\xi + \lambda(\text{tr}\,\xi)\mathbb{I}_n$, with the Lamé moduli λ and μ,
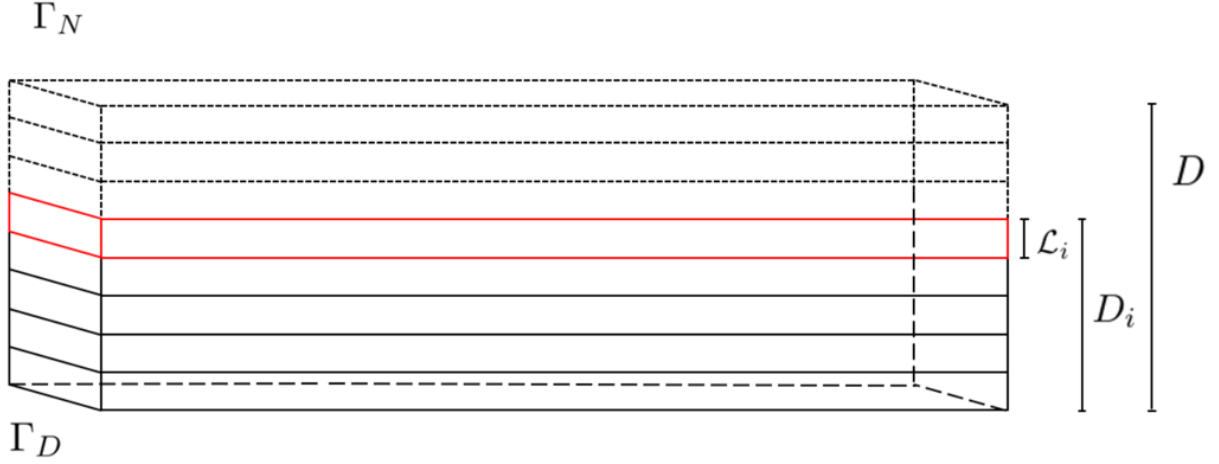
Figure 1: Intermediate domains D_i in the build chamber D

and the identity matrix $\mathbb{I}_n$. The elastic strain tensor, denoted by ϵ_e in (1), is defined as $\epsilon_e = e(u) = \frac{1}{2}(\nabla u + \nabla u^T)$. The stress tensor σ_i in ω_i is thus the sum of the elastic stress and of the inherent stress. The inherent strain $\epsilon^*_{\mathcal{L}_i}(x)$ is applied only in the last layer $\mathcal{L}_i$. The reason is that most strains induced by the process result from the shrinkage of the last melted layer during its cooling. In this model, it is thus assumed that this shrinkage occurs in $\mathcal{L}_i$ and the previous domain D_{i-1} is at rest temperature when the new layer is added. In other words, the heat brought by the laser beam has a mechanical impact only in the last layer $\mathcal{L}_i$ according to this model. The layers M_i are macro layers and do not represent the very thin true layers in the actual powder bed. A representative scheme of the intermediate shape ω_i is shown in Figure 2.
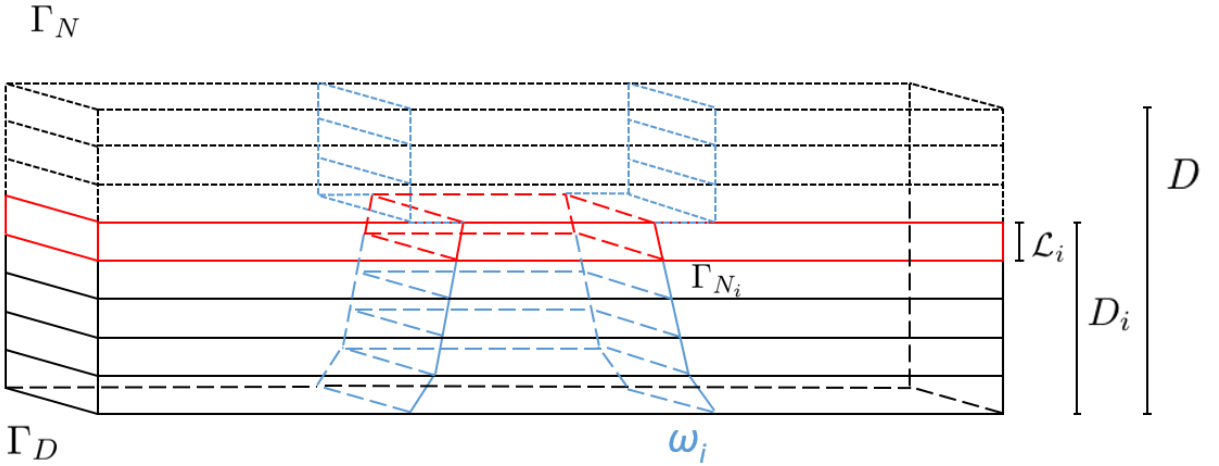

Figure 2: Layer by layer construction of the part ω in the build chamber D

To illustrate this inherent strain model, we perform a numerical simulation of the construction of a simple cube of side length 50mm, using the finite element software FreeFEM [19]. The Young modulus is set to 125 GPa, the Poisson coefficient to 0.3 and the build chamber D is divided into $M = 50$ macro-layers horizontal layers. A calibration step has not been made for the results shown in this Section (contrary to what we shall do in Section 7). However, we choose the same inherent strain tensor ϵ^* as the one used in the

commercial process simulation software *Simufact Additive* ®[1], also using the inherent strain model. This tensor has been previously calibrated by expert users with the same mechanical parameters and mesh size. This inherent strain tensor is

$$\epsilon^* = \begin{bmatrix} -0.0001 & 0 & 0 \\ 0 & -0.0001 & 0 \\ 0 & 0 & 0 \end{bmatrix} \tag{4}$$

In view of (4), the inherent strains are imposed isotropically on the plane layer at each layer. The result of the simulation is displayed on Figure 3 (left), where the Von Mises stress is computed and lumped at each layer. This hypothesis stating that the final stress state is the sum of all the intermediate stress states, for $1 \le i \le M$, is an approximation which can only be used in a linear elasticity setting.

To assess our results, a comparison is made with the software *Simufact Additive* ®. The exact same geometry and set of parameters (mechanical parameters, number of layers, inherent strain tensor) are considered and the Von Mises field $\sigma_{vm}(x)$ is computed such that

$$\sigma_{vm} = \left| \sum_{i=1}^{M} 2\mu e(u_i)_D \right|, \tag{5}$$

with u_i the solution of (3) computed in ω_i and extended by 0 outside. Recall that the deviatoric part of a $n \times n$ square matrix ξ is $\xi_D = \xi - \frac{tr(\xi)}{n}\mathbb{I}_n$. The result is displayed in Figure 3 (right).
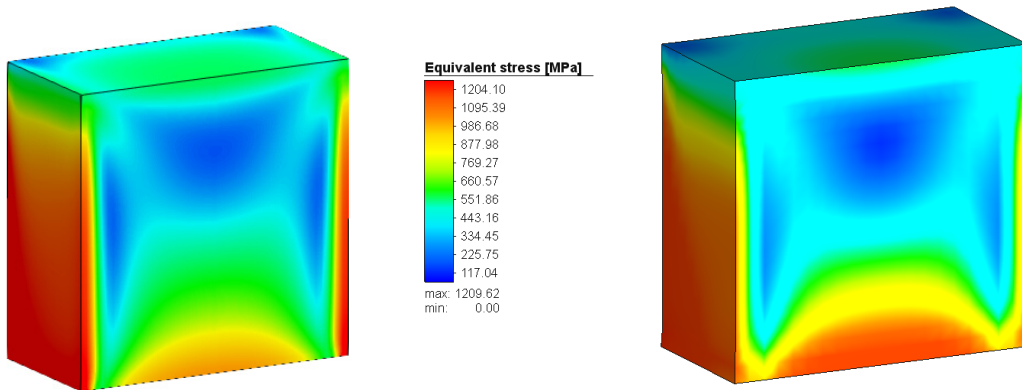

Figure 3: Visualization of the Von Mises criterion at the mid section of a cube build with 50 layers, computed with FreeFEM (left) and Simufact Additive (right)

As already said, the inherent strain model is only valid in the elastic domain, so the strains are overestimated above the limit of elasticity. To compare our results with the simulation of *Simufact Additive* ®, we first apply a maximum threshold to the Von Mises criterion obtained with our model. This maximum threshold is chosen equal to the maximum value of the Von Mises criterion obtained with *Simufact Additive* ®, which uses a plasticity model. With this post-treatment, our numerical result shows qualitative good agreement with the one of *Simufact Additive* ®.

---

[1]https://www.simufact.com/additive-manufacturing.html

3 Optimization problem

In this section we optimize a part ω concurrently for its final use (see Subsection 3.1) and for its behavior during the manufacturing process (see Subsection 3.2). The coupled optimization problem is described in Subsection 3.3. No supports are involved for the moment.

3.1 Final-use problem

For its final use, the part ω is submitted to some loads f with boundary conditions which have nothing to do with the inherent strain model (3) which merely determines its deformation during the building process. Therefore, the part boundary $\partial\omega$ is decomposed in disjoint subsets $\partial\omega = \Gamma_{D_f} \cup \Gamma_{N_f} \cup \Gamma$ and a Sobolev space of kinematically admissible displacements is defined as

$$H^1_{\Gamma_{D_f}}(\omega) := \left\{ v \in H^1(\omega)^n \text{ such that } v = 0 \ \text{ on } \ \Gamma_{D_f} \right\}.$$

For given loads $f \in L^2(\Gamma_{N_f})^n$, the final-use problem amounts to find the displacement field u_{fin} which is the unique solution in $H^1_{\Gamma_{D_f}}(\omega)$ of

$$\begin{cases} -\text{div}(Ae(u_{\text{fin}})) &=& 0 & \text{on } \omega, \\ Ae(u_{\text{fin}})n &=& 0 & \text{on } \Gamma, \\ Ae(u_{\text{fin}})n &=& f & \text{on } \Gamma_{N_f}, \\ u_{\text{fin}} &=& 0 & \text{on } \Gamma_{D_f}, \end{cases} \tag{6}$$

where A is the same isotropic elasticity tensor, as in the previous section. Note that the boundaries Γ_{N_f} and Γ_{D_f} are not necessarily the same than the ones for the manufacturing problem (3) and that there is no layer-by-layer process in (6).

The performance of the part ω for its final use is evaluated by the compliance, defined as

$$C(\omega) = \int_{\Gamma_{N_f}} f \cdot u_{\text{fin}} \, ds, \tag{7}$$

where u_{fin} is the solution of (6). Of course, other criteria could have been chosen.

3.2 Manufacturing problem

A criterion depending on each layer is defined, depending on all intermediate solutions of the layer-by-layer problem (3):

$$J(\omega) = \sum_{i=1}^{M} \int_{\omega_i} j(u_i) \, dx, \tag{8}$$

where $j : \mathbb{R}^n \mapsto \mathbb{R}$ is a smooth function. The goal of this criterion is to evaluate the manufacturability of the part (see examples in the next sections).

To compute the sensitivity of (8) in the next subsection, an adjoint problem for (3) is required. For $1 \le i \le M$, we define an adjoint p_i, which is the unique solution in $H^1_{\Gamma_D}(\omega_i)$ of

$$\begin{cases} -\text{div}(Ae(p_i)) &=& -j'(u_i) & \text{in } \omega_i, \\ (Ae(p_i))n &=& 0 & \text{on } \Gamma_{N_i}, \\ p_i &=& 0 & \text{on } \Gamma_D. \end{cases} \tag{9}$$

3.3 Coupled optimization problem

Our goal is to reduce the manufacturing defects by optimizing the shape of the part, while ensuring good performances for its final use, after the manufacturing, all together with a volume constraint. To set up a coupled optimization problem, we introduce a reference shape ω_{ref} which has been obtained by minimizing the compliance (7) for its final use, with a volume constraint $|\omega_{\text{ref}}|$. This shape ω_{ref} gives a reference value for the compliance which should not increase too much if the part manufacturability is optimized.

More precisely, introducing a small coefficient $k > 0$, allowing a slight increase of the compliance for the final use, we consider the following minimization problem

$$
\begin{aligned}
\min_{\omega \subset D} \quad & J(\omega) \\
\text{s.t.} \quad |\omega| \ &= \ |\omega_{\text{ref}}|, \\
C(\omega) \ &\leq \ (1+k)C(\omega_{\text{ref}}),
\end{aligned}
\tag{10}
$$

where the compliance $C(\omega)$ is defined by (7) and the manufacturing criterion $J(\omega)$ is defined by (8). Note that there are two state equations for this optimization problem: (3) for the manufacturing process (with solutions u_i) and (6) for the final use (with solution u_{fin}).

For the numerical resolution of (10), we shall rely on constrained gradient algorithms. Therefore, we need to compute so-called shape derivatives of the functions $C(\omega)$ and $J(\omega)$, by relying on the Hadamard method of shape sensitivity [1]. The main idea is to study variations of a shape ω, displaced by a vector field $\theta(x)$. More precisely, for any $\theta \in W^{1,\infty}(D, \mathbb{R}^n)$, the deformation of ω by θ is defined by $\omega_\theta = (\text{Id} + \theta)\omega$. Computing a shape derivative amounts to differentiate with respect to θ. Note that in the sequel we force the vector fields θ to vanish on the Dirichlet boundaries and on the boundaries where loads are applied (to simplify the formulas of the derivatives). In other words, only the traction-free boundaries are allowed to move in the optimization process.

The shape derivative of the compliance is a well-known result [8]. In particular, it features no adjoint (compliance minimization is a self-adjoint problem).

Proposition 3.1. *For any vector field $\theta \in W^{1,\infty}(D, \mathbb{R}^n)$ which vanishes on $\Gamma_{N_f} \cup \Gamma_{D_f}$, the shape derivative of $C(\omega)$ defined by (7) is*

$$
C'(\omega)(\theta) = \ -\int_{\partial\omega} \theta \cdot n \left(A(e(u_{\text{fin}})) : e(u_{\text{fin}}) \right) \, ds.
\tag{11}
$$

The theory of shape derivation in the context of a layer-by-layer model (3) was established in [5]. As a consequence, the shape derivative of the manufacturing criterion $J(\omega)$ is given by the next result.

Proposition 3.2. *For any vector field $\theta \in W^{1,\infty}(D, \mathbb{R}^n)$ which vanishes on Γ_D, the shape derivative of $J(\omega)$ defined by (8) is*

$$
J'(\omega)(\theta) = \ \sum_{i=1}^{M} \int_{\partial\omega_i \cap \partial\omega} \theta \cdot n \left(j(u_i) + \left(A(e(u_i) + \epsilon^*_{\mathcal{L}_i}) \right) : e(p_i) \right) \, ds
\tag{12}
$$

with p_i the adjoint state, solution of (9).

Proof. Céa's fast derivation method [16] is used to compute the shape derivative of the objective function. The Lagrangian is first introduced being the sum of the objective

8

function and of the variational formulation of problems (3) and (9). It depends on the shape ω and functions $\hat{u}_i, \hat{p}_i \in H^1_{\Gamma_D}(\omega_i)$:

$$\mathcal{L}(\omega, \hat{u}_i, \hat{p}_i) = \sum_{i=1}^{M} \int_{\omega_i} j(\hat{u}_i) \, dx + \sum_{i=1}^{M} \int_{\omega_i} A\left(e(\hat{u}_i) + \epsilon^*_{\mathcal{L}_i}\right) : e(\hat{p}_i) \, dx.$$

Note that the variables $\hat{u}_i, \hat{p}_i$ are not solutions of the problem (3) and (9). By definition, differentiating $\mathcal{L}$ with respect to $\hat{p}_i$, in the direction of a test function $\phi_i \in H^1_{\Gamma_D}(\omega_i)$, and looking for a critical point, leads to the variational formulation of the manufacturing problem (3), namely

$$\frac{\partial \mathcal{L}(\omega, \{\hat{u}_i\}, \{\hat{p}_i\})}{\partial \hat{p}_i}(\phi_i) = \int_{\omega_i} \left(A(e(\hat{u}_i) + \epsilon^*_{\mathcal{L}_i})\right) : e(\phi_i) \, dx = 0. \tag{13}$$

On the other hand, differentiating $\mathcal{L}$ with respect to $\hat{u}_i$, in the direction of a test function $\phi_i \in H^1_{\Gamma_D}(\omega_i)$, and equating to zero at the optimal point, yields

$$\frac{\partial \mathcal{L}(\omega, \{\hat{u}_i\}, \{\hat{p}_i\})}{\partial \hat{u}_i}(\phi_i) = \int_{\omega_i} \left(Ae(\phi_i) : e(\hat{p}_i)\right) \, dx + \int_{\omega_i} j'(\hat{u}_i) \cdot \phi_i dx = 0, \tag{14}$$

which is the variational formulation of the adjoint problem associated to the problem (3). Finally, assuming that the solutions u_i are shape differentiable and differentiating $\mathcal{L}$ with respect to ω in the direction of the vector field θ, gives the shape derivative of the objective function

$$\begin{aligned}\frac{\partial \mathcal{L}(\omega, \{u_i\}, \{p_i\})}{\partial \omega}(\theta) = \ &\sum_{i=1}^{M} \int_{\partial \omega_i \cap \partial \omega} j(u_i)\theta \cdot n \, ds \\ &+ \sum_{i=1}^{M} \int_{\partial \omega_i \cap \partial \omega} \left(A(e(u_i) + \epsilon^*_{\mathcal{L}_i})\right) : e(p_i)\theta \cdot n \, ds,\end{aligned}$$

which is the desired result (12). Note that the surface integrals are carried on $\partial \omega_i \cap \partial \omega$ and not on $\partial \omega_i$ because it is ω which is deformed by θ and $\omega_i = \omega \cap D_i$. $\qquad \square$

4 Numerical framework

This section is a brief review of the main ingredients for our computations. More details can be found in [6]. All partial differential equations are simulated with the finite element software FreeFEM [19]. The computations are made on a 2.50 GHz Intel(R) Xeon(R) CPU.

4.1 Extension and regularization of the shape derivative

For any objective function $J(\omega)$, its shape derivative reads, for $\theta \in W^{1,\infty}(D, \mathbb{R}^n)$,

$$J'(\omega)(\theta) = \int_{\partial \omega} j\theta \cdot n \, ds,$$

where $j(x)$ depends on the solutions of the direct and adjoint problems. Therefore, it is possible to choose $\theta = -jn$ as a descent direction to decrease the objective function.

However, the integrand j and the normal vector n are defined only on the boundary $\partial\omega$, while in numerical practice it is required to know the vector field θ everywhere in the domain D. The level set method already gives an extension of the normal n and it remains to extend the scalar field j. In passing it is also regularized for a better convergence of the gradient algorithm. Following [8], [6], we compute the extension $\mathcal{V} \in H^1(D)$ as the unique solution of the variational formulation

$$\int_D (\varepsilon^2 \nabla\mathcal{V} \cdot \nabla W + \mathcal{V}W)\, dx = \int_{\partial\omega} jW ds \ \text{ for all } \ W \in H^1(D),$$

where the regularization parameter $\varepsilon > 0$ is typically the mesh size. Eventually, $\theta = -\mathcal{V}n$ guarantees a descent direction such that $J'(\omega)(-\mathcal{V}n) \leq 0$.

4.2 Level set Method

In order to parametrize the shape ω in a fixed computational mesh, the level set method is used [31]. The shape ω is defined by a level set function $\varphi : D \to \mathbb{R}$ satisfying

$$\begin{cases} \varphi(x) &= 0 \ \text{ if } \ x \in \partial\omega \cap D, \\ \varphi(x) &< 0 \ \text{ if } \ x \in \omega, \\ \varphi(x) &> 0 \ \text{ if } \ x \in D\backslash\omega. \end{cases}$$

Given $\mathcal{V}$ a scalar normal velocity, calculated through shape derivative analysis, the level set function is updated by solving the following Hamilton-Jacobi equation, or transport equation:

$$\frac{\partial\varphi}{\partial t} + \mathcal{V}|\nabla\varphi| = 0, \tag{15}$$

The computation of (15) is made with the software Advect from the ISCD Toolbox [15]. The level set function obtained after this advection step may not be equal to a signed function anymore. Thus, a re-distanciation procedure is performed at each iteration with the *distance* function in FreeFEM [19] so that the level set function φ remains the signed distance function to the actual shape.

4.3 Optimization Algorithm

To solve the constrained optimization problem (10) we rely on an augmented Lagrangian algorithm. Following [28] (section 17.4), it is written:

$$\begin{aligned} \mathcal{L}(\omega, \lambda_v, \mu_v, \lambda_c, \mu_c) = J(\omega) \ &-\lambda_v\left(|\omega| - |\omega_{\text{ref}}|\right) + \frac{\mu_v}{2}\left(|\omega| - |\omega_{\text{ref}}|\right)^2 \\ &-\lambda_c\max\left(C(\omega) - (1+k)C(\omega_{\text{ref}}), -\frac{\lambda_c}{\mu_c}\right) \\ &+\frac{\mu_c}{2}\left|\max\left(C(\omega) - (1+k)C(\omega_{\text{ref}}), -\frac{\lambda_c}{\mu_c}\right)\right|^2, \end{aligned} \tag{16}$$

where λ_v and λ_c are the Lagrange multipliers for the volume and compliance constraints, respectively, while μ_v and μ_c are the penalization coefficients for the volume and compliance constraints, respectively. Recall that $k > 0$ is a coefficient allowing for a small increase of the final use compliance in (10). At each iteration j, the Lagrange multipliers λ_v and λ_c are updated as :

$$\lambda_v^{j+1} = \lambda_v^j - \mu_v \left(|\omega| - |\omega_{\text{ref}}| \right),$$
$$\lambda_c^{j+1} = \lambda_c^j + \mu_c \max \left(C(\omega) - (1+k)C(\omega_{\text{ref}}), -\frac{\lambda_c}{\mu_c} \right).$$

Eventually, the optimization procedure is the following.

- **Initialisation.** An initial level set φ_0 function is chosen.

- **Optimization loop.** At iteration $j \geq 0$, the various direct and adjoint problems are solved with the current shape φ_j, allowing to evaluate the cost function, constraints and the shape derivative. This gives a velocity $\mathcal{V}_j(x)$ used to solve the Hamilton-Jacobi equation and obtain the new level set function φ_{j+1}. If the value of the augmented Lagrangian decreases, then the iteration is accepted, else the iteration is rejected and started again with a smaller step size. At each iteration, the level set function is reinitialized as the signed function of the current shape ω_j.

- **Convergence.** When the L^2-norm of $\mathcal{V}$ is small enough (in this work, a threshold 10^{-6} is used), the optimization algorithm is stopped as the convergence is reached.

5 Numerical test cases

In this section we numerically solve the optimization problem (10), introduced in Section 3, for two different choices of the objective function $J(\omega)$. In both cases, the constraint on the final-use compliance $C(\omega)$ is the same.

Throughout this section we consider a MBB beam, optimized for its final use with loads f and which must be properly manufactured in a layer-by-layer process with $M = 20$ layers. The boundary conditions and the loading for the final use are depicted in Figure 4. The computational domain D is of size $[0, 30mm] \times [0, 5mm] \times [0, 10mm]$, discretized with 40500 nodes and corresponding to a quarter of a MBB beam, two vertical symmetries are applied. The values of the mechanical parameters are $E = 125$ GPa and $\nu = 0.3$. The force $f = (0, 0, -0.5)$ is applied on a $5mm^2$ band centered on the top boundary of the domain. The Dirichlet boundary Γ_{D_f} is located on the tips of the bottom boundary, on two $2.5mm^2$ bands. Finally, the inherent strain tensor ϵ^* used for our simulation is (4), as in Section 2.

A reference shape ω_{ref} is first obtained by minimizing compliance for its final use with a volume constraint $|\omega_{\text{ref}}| = 0.3|D|$. It is displayed in Figure 5. All our optimization processes will start from this reference shape.
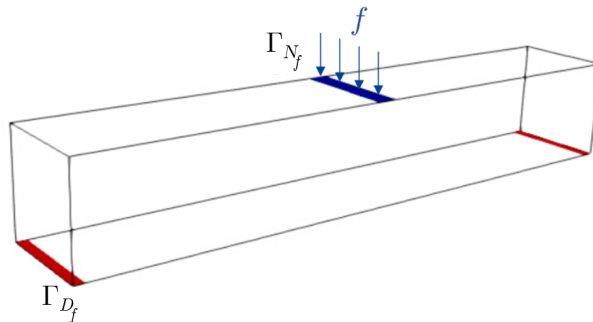

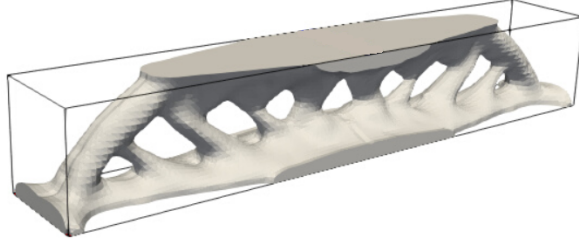Figure 4: Boundary conditions and loading for the MBB beam

Figure 5: Optimal compliance shape ω_{ref} for the MBB beam

5.1 Minimizing the vertical displacements

As already explained, each layer endures a thermal shrinkage during the cooling phase. The non-supported tips of these layers may deform, resulting in a poor surface quality. Some of the tips may even deform beyond the powder bed of the next layer and may stop the machine if a metal recoater is used (see Figure 6). If a soft recoater is used, these tips may torn it and disrupt the powder bed spreading.
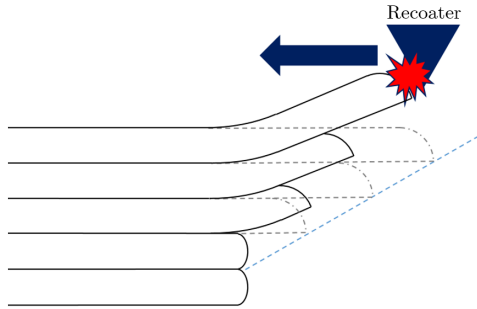

Figure 6: Sketch of the layer deformation beyond the powder bed, which can stop the layer deposition.

To prevent this phenomenon we introduce a first objective function $J_1(\omega)$ which takes into account the vertical components of displacements u_i, computed with (3) in each intermediate shape ω_i. It is defined by

$$J_1(\omega) = \sum_{i=1}^{M} \int_{\omega_i} j_1(u_i)dx \quad \text{with} \quad j_1(u_i) = |\max(0, u_i \cdot e_n)|^2 \chi_{\mathcal{L}_i}, \tag{17}$$

where e_n is the vertical build direction. Note that the influence of each displacement u_i is restricted to its corresponding layer $\mathcal{L}_i$ in (17).

The initialization of the optimization process for (10) is the reference shape ω_{ref}, displayed on Figure 5. For this initial shape we solve (3) with $M = 20$ layers and compute the sum of the displacements u_i as

$$u(x) = \sum_{i=1}^{M} u_i(x)\chi_{\mathcal{L}_i}(x).$$

The vertical component of u for ω_{ref} is plotted on Figure 7. One can notice that the vertical displacement is larger around the overhanging surfaces. This further motivates the use of model (3) as it is in accordance with experimental results made on these critical areas [34].
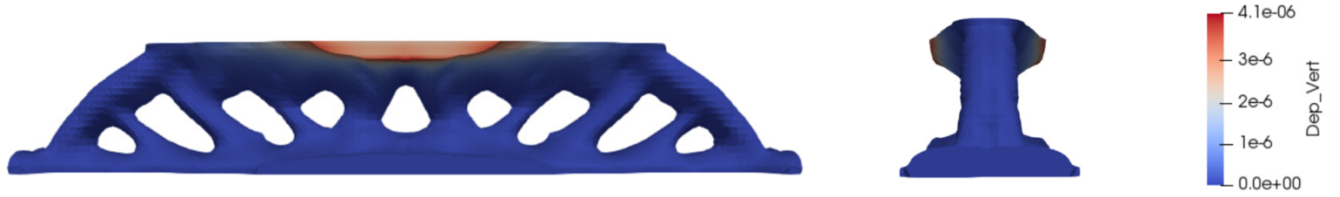
Figure 7: Sum of the vertical displacements for the initial shape ω_{ref}, side view (left) and front view (right).

Solving the optimization problem (10) with $J(\omega) = J_1(\omega)$ and $k = 0.01$, starting from ω_{ref}, yields an optimized shape, shown on Figure 8. One can clearly see that the overhang parts have disappeared and the associated volume has been redistributed on the vertical bars of the beam, preserving its rigidity. Convergence curves for the rescaled functions $J(\omega)$, $C(\omega)$ and volume are displayed on Figure 9: the amount of vertical displacements has been drastically reduced.
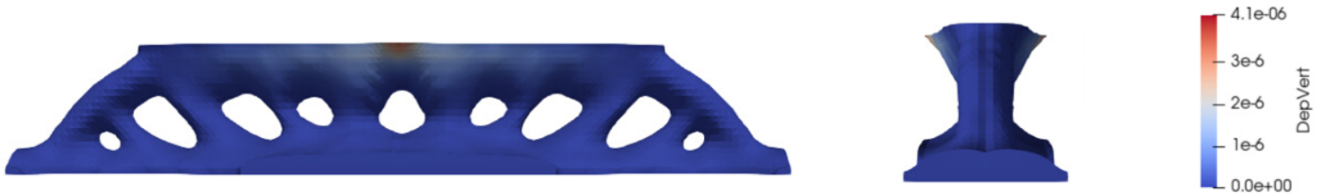

Figure 8: Sum of the vertical displacements for the optimized shape, side view (left) and front view (right).
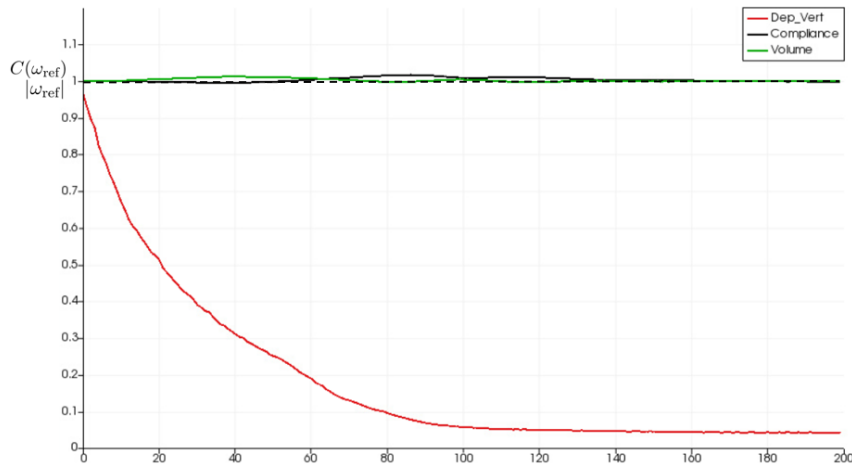

Figure 9: Convergence history for the objective function $J_1(\omega)$ (red), the compliance $\mathrm{C}(\omega)$ (black) and the volume $|\omega|$ (green).

5.2   Minimizing a Von Mises criterion

We now choose another objective function $J(\omega)$, involving the stress field, which of course implies a new definition of the adjoint problem (9). Define the Von Mises field, denoted

13

$\sigma_{vm}(x)$, by:

$$\sigma_{vm} = \left| \sum_{i=1}^{M} 2\mu e(u_i)_D \right|, \tag{18}$$

with u_i being the solution of (3) computed in ω_i and extended by 0 outside. Formula (18) takes into account each step of the manufacturing process, giving information on the stress state inside the part after construction. As stated in Section 2, our model gives proper predictions in the elastic domain, and overestimates the strain above the limit of elasticity. An interesting point would be to reduce as much as possible the region where σ_{vm} is the largest. This region is not properly taken into account by our simulation model which ignores plastic deformations, although they frequently occur in additive manufacturing. There regions of large stress are undesired and to minimize their volume, we propose the following criterion, considering a p-norm (to avoid any confusion with the adjoint state already denoted by p, the exponent of the norm is called $\alpha > 0$). This criterion reads

$$J_2(\omega) = \left(\int_\omega j_2(e(u)) \, dx \right)^{\frac{1}{\alpha}} \text{ with } j_2(e(u)) = |\sigma_{vm}|^{2\alpha}. \tag{19}$$

Proposition 5.1. *The shape derivative of $J_2(\omega)$ is still given by (12) but with a new adjoint problem, defined for $1 \le i \le M$, by*

$$\begin{cases} -\operatorname{div}(Ae(p_i)) &= \operatorname{div}\left(K_1 |\sigma_{vm}|^{2\alpha-2} \sum_{j=1}^{M} \sigma_{j,D} \right) &\text{in } \omega_i, \\ (Ae(p_i))n &= -\left(K_1 |\sigma_{vm}|^{2\alpha-2} \sum_{j=1}^{M} \sigma_{j,D} \right) n &\text{on } \Gamma_{N_i}, \\ p_i &= 0 &\text{on } \Gamma_D. \end{cases} \tag{20}$$

with $K_1 = 4\mu \left(\int_\omega |\sigma_{vm}|^{2\alpha} \, dx \right)^{\left(\frac{1}{\alpha}-1\right)}$ and $\sigma_{j,D} = 2\mu e(u_j)_D$.

Proof. The proof is very similar to that of Proposition 3.2 and we only give the main new ingredients. The associated Lagrangian defined for ω and the family of functions $\{\hat{u}_i\}, \{\hat{p}_i\} \in H^1_{\Gamma_D}(\omega_i)$, for $1 \le i \le M$, is written as:

$$\mathcal{L}(\omega, \{\hat{u}_i\}, \{\hat{p}_i\}) = \left(\int_\omega j_2(e(u)) \, dx \right)^{\frac{1}{\alpha}} + \sum_{i=1}^{M} \int_{\omega_i} A(e(\hat{u}_i) + \epsilon^*_{\mathcal{L}_i}) : e(\hat{p}_i)) \, dx. \tag{21}$$

Differentiate with respect to $\hat{u}_i$ in the direction of a test function $\phi_i \in H^1_{\Gamma_D}(\omega_i)$ and searching for the critical point, we get

$$\begin{aligned} \frac{\partial \mathcal{L}(\omega, \{\hat{u}_i\}, \{\hat{p}_i\})}{\partial \hat{u}_i}(\phi_i) = {}& \frac{1}{\alpha} \left(\int_\omega j_2(e(\hat{u})) \, dx \right)^{\left(\frac{1}{\alpha}-1\right)} \left(\int_\omega j'_2(e(\hat{u})) \cdot e(\phi_i) \, dx \right) \\ & + \int_{\omega_i} (Ae(\phi_i) : e(\hat{p}_i)) \, dx = 0. \end{aligned} \tag{22}$$

More precisely,

$$\begin{aligned} \frac{1}{\alpha} \left(\int_\omega |\sigma_{vm}|^{2\alpha} \, dx \right)^{\left(\frac{1}{\alpha}-1\right)} & \left(\int_\omega \alpha |\sigma_{vm}|^{2\alpha-2} 4\mu \left(\sum_{j=1}^{M} \sigma_{j,D} \right) : e(\phi_i) \, dx \right) \\ & + \int_{\omega_i} Ae(\phi_i) : e(\hat{p}_i) \, dx = 0, \end{aligned} \tag{23}$$

which is the variational formulation of the layer-by-layer adjoint problem (20). □

14

The Von Mises field σ_{vm} is computed on the initial shape ω_{ref}, displayed on Figure 5, for $M = 20$ layers: it is plotted on Figure 10. Solving the optimization problem (10) with $J(\omega) = J_2(\omega)$, $\alpha = 12$, $k = 0.04$ (the allowed increase in the compliance constraint of (10)), starting from ω_{ref}, yields an optimized shape, shown on Figure 11. On the same figure is plotted the Von Mises field σ_{vm} with the same color scale as in Figure 10. The maximal value of σ_{vm} has been reduced.
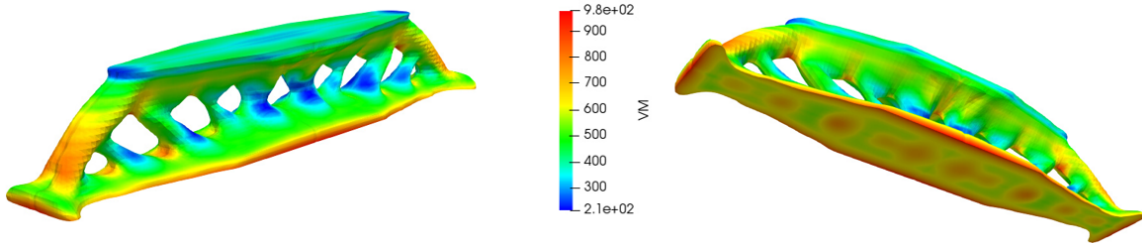

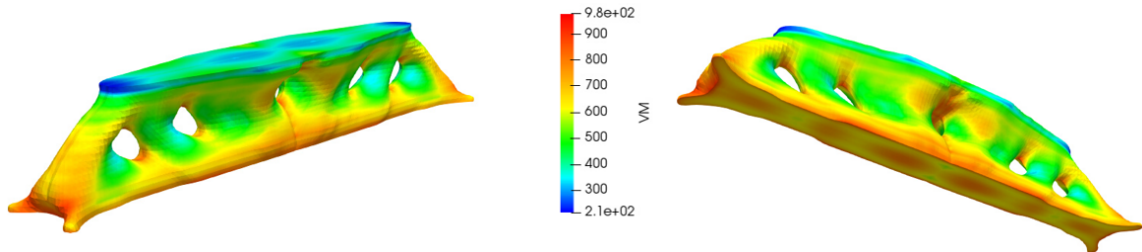Figure 10: Von Mises field for the initial shape ω_{ref}. Maximum value: 980 MPa

Figure 11: Von Mises field after optimization with $\alpha = 12$. Maximum value: 940 MPa

A classical result in SLM manufacturing is the presence of important stress at the junction of the part and the baseplate [24]. As the objective function (19) focuses, for large exponent α, on the highest values of the Von Mises field, the optimized shape features smaller regions where it is clamped to the baseplate while preserving as much as possible the initial compliance. One can observe the formation of two horns at the tips of the beam, keeping contact with the Dirichlet boundary conditions of the final-use problem (6). Convergence curves are plotted in Figure 12.
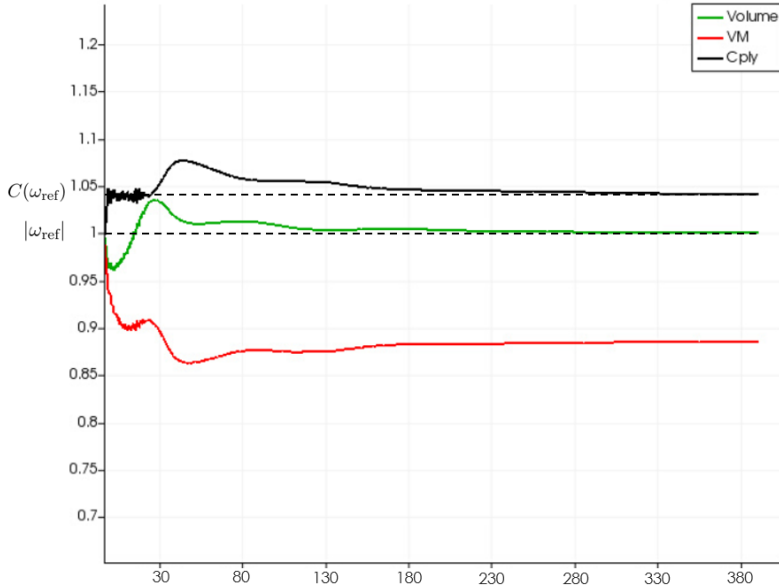
Figure 12: Convergence history for the objective function $J_2(\omega)$ (red), the compliance $C(\omega)$ (black) and the volume $|\omega|$ (green).

6 Minimization of residual deformation after baseplate separation

We now depart from the setting of Section 3 and consider a new optimization problem with a new state equation. The goal is to reduce the part deformation once it is separated from the baseplate. The shape of the part ω is again the only optimization variable in this section.

6.1 Model of baseplate separation

The separation of the part ω from its baseplate is a complex phenomenon to accurately simulate, not to mention to optimize. Therefore, we introduce a very simplified model which could be enriched in some future work. Instead of taking into account the whole cutting process, we focus on a single snapshot where the part is partially separated from the baseplate. Of course, the amount of separation is somehow arbitrary. Our simplified model goes as follows.

In a first step, the building process of the part ω is simulated by solving the inherent strain model (3), as in the previous sections. It yields a family of intermediate displacements u_i, $1 \leq i \leq M$.

In a second step, the part ω has been partly separated from the baseplate, so that it is clamped on a subset $\Gamma_{D_{\text{cut}}} \subset \Gamma_D$ of the baseplate. The remaining part $\Gamma_{N_{\text{cut}}} = \Gamma_D \setminus \Gamma_{D_{\text{cut}}}$ is now a traction-free boundary. Associated to this new Dirichlet boundary, we introduce a new Sobolev space of kinematically admissible displacement

$$H^1_{\Gamma_{D_{\text{cut}}}}(\omega) := \left\{ v \in H^1(\omega)^n \text{ such that } v = 0 \text{ on } \Gamma_{D_{\text{cut}}} \right\},$$

which is different from the previous space (2), associated to Γ_D. A pre-stress state is deduced from solving (3) in the first step and it is used as a load for the mechanical

16

problem of the second step, modeling the baseplate separation (see at the bottom of Figure 13): find the displacement field v, solution in $H^1_{\Gamma_{D_{\text{cut}}}}(\omega)$ of

$$
\begin{cases}
-\operatorname{div}\left(Ae(v) + \sum_{j=1}^{M} Ae(u_j)\right) &= 0 \quad \text{in } \omega, \\
\left(Ae(v) + \sum_{j=1}^{M} Ae(u_j)\right)n &= 0 \quad \text{on } \partial\omega \setminus (\Gamma_{N_{\text{cut}}} \cup \Gamma_{D_{\text{cut}}}) \\
Ae(v)n &= 0 \quad \text{on } \Gamma_{N_{\text{cut}}}, \\
v &= 0 \quad \text{on } \Gamma_{D_{\text{cut}}}.
\end{cases}
\tag{24}
$$

where u_j is extended by 0 outside ω_j. This second problem (24) models a partial cut from the baseplate by changing the Dirichlet boundary Γ_D into a smaller region $\Gamma_{D_{\text{cut}}}$. The solution v is the deflection of the part ω, after partial separation from the baseplate, consequence of the residual inherent strains modeled by the solutions u_i of (3). Remark that, in view of (3),

$$
-\operatorname{div} \sum_{j=1}^{M} Ae(u_j) = \operatorname{div} \sum_{j=1}^{M} A\epsilon^* \chi_{\mathcal{L}_i}(x) = \operatorname{div} A\epsilon^* = 0,
$$

but the Neumann boundary condition on $\partial\omega \setminus (\Gamma_{N_{\text{cut}}} \cup \Gamma_{D_{\text{cut}}})$ does not vanish and is not homogeneous. If there is no cut, namely $\Gamma_{N_{\text{cut}}} = \emptyset$, the solution v of (24) is not zero but is extremely small (typically 3 orders of magnitude smaller on the arch example of Subsection 6.2).
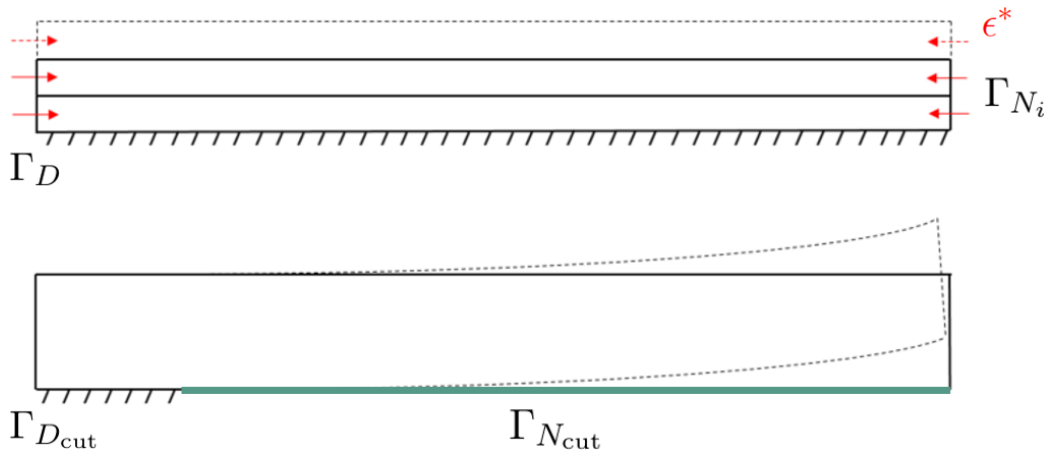

Figure 13: Sketch of the geometrical setting for (3) (top) and (24) (bottom), modeling the baseplate separation and stress relaxation

With this new model we consider a new optimization problem, which is somehow similar to the previous one (10) in the sense that it still involves the final-use compliance and the volume as constraints. More precisely, in view of a reference shape ω_{ref} (typically obtained by minimizing the final-use compliance), the optimization problem reads

$$
\begin{aligned}
\min_{\omega \subset D} \quad & J_3(\omega) \\
\text{s.t.} \quad & |\omega| = |\omega_{\text{ref}}|, \\
& C(\omega) \leq (1+k)C(\omega_{\text{ref}}),
\end{aligned}
\tag{25}
$$

where the final-use compliance $C(\omega)$ is defined by (7) and the separation criterion $J_3(\omega)$ is defined by

$$
J_3(\omega) = \int_\omega j_3(v)dx \quad \text{with} \quad j_3(v) = |\max(0, v \cdot e_n)|^2,
\tag{26}
$$

where v is the displacement, solution of (24). The novelty of (25), compared to (10), is that it features three state equations, namely (3) and (24) (for evaluating $J_3(\omega)$) and (6) (for evaluating $C(\omega)$).

As usual, the state equation (24) requires an adjoint problem, which is

$$\begin{cases} -\text{div}(Ae(\eta)) & = & -j_3'(v) & \text{in } \omega, \\ (Ae(\eta))n & = & 0 & \text{on } \partial\omega \setminus \Gamma_{D_{\text{cut}}}, \\ \eta & = & 0 & \text{on } \Gamma_{D_{\text{cut}}}. \end{cases} \tag{27}$$

Since the objective function is different, the first state equation (3) is associated to another adjoint problem, different from (9). Its variationnal formulation reads: find $p_i \in H^1_{\Gamma_D}(\omega_i)$ such that, for any test function $\phi_i \in H^1_{\Gamma_D}(\omega_i)$,

$$\int_{\omega_i} Ae(p_i) : e(\phi_i)\, dx = -\int_{\omega_i} Ae(\eta) : e(\phi_j)\, dx + \int_{\Gamma_{N_{\text{cut}}}} Ae(\phi_j)n \cdot \eta\, ds. \tag{28}$$

The solution p_i satisfies the following strong from

$$\begin{cases} -\text{div}(Ae(p_i)) & = & \text{div}\,(Ae(\eta)) & \text{in } \omega_i, \\ (Ae(p_i))n & = & -(Ae(\eta))n & \text{on } \Gamma_{N_i} \setminus \Gamma_{N_{\text{cut}}}, \\ p_i & = & 0 & \text{on } \Gamma_D, \end{cases}$$

with a non-standard boundary condition on $\Gamma_{N_{\text{cut}}}$.

Proposition 6.1. *For any vector field $\theta \in W^{1,\infty}(D, \mathbb{R}^n)$ which vanishes on Γ_D, the shape derivative of $J_3(\omega)$ is given by*

$$\begin{aligned} J_3'(\omega)(\theta) & = \int_{\partial\omega} \theta \cdot n \left(j_3(v) + (Ae(v) + \sum_{j=1}^{M} Ae(u_j)) : e(\eta) \right) ds \\ & + \sum_{i=1}^{M} \int_{\partial\omega \cap \omega_i} \theta \cdot n \left(Ae(u_i) + \epsilon^*_{\mathcal{L}_i} \right) : e(p_i)\, ds \end{aligned} \tag{29}$$

where p_i is the adjoint of u_i and η is the adjoint of v.

Proof. The proof is again very similar to that of Proposition 3.2 and we only give the main new ingredients. Introduce the Lagrangian, defined as the sum of the objective function and the two variational formulations of (3) and (24):

$$\begin{aligned} \mathcal{L}(\omega, \hat{v}, \hat{\eta}, \{\hat{u}_i\}, \{\hat{p}_i\}) = & \int_{\omega} j_3(\hat{v}) dx + \int_{\omega} \left(Ae(\hat{v}) + \sum_{j=1}^{M} Ae(\hat{u}_j) \right) : e(\hat{\eta})\, dx \\ & - \int_{\Gamma_{N_{\text{cut}}}} \sum_{j=1}^{M} Ae(\hat{u}_j)n \cdot \hat{\eta}\, ds \\ & + \sum_{i=1}^{M} \int_{\omega_i} (Ae(\hat{u}_i) + \epsilon^*_{\mathcal{L}_i}) : e(\hat{p}_i)\, dx. \end{aligned} \tag{30}$$

Differentiating $\mathcal{L}$ with respect to $\hat{v} \in H^1_{\Gamma_{D_{\text{cut}}}}(\omega)$ leads to the variational formulation of the adjoint problem (27). Differentiating $\mathcal{L}$ with respect to $\hat{u}_i$ gives the variational formulation of the adjoint problem (28). Assuming that the solutions v, u_i are shape differentiable and differentiating $\mathcal{L}$ with respect to ω in the direction of the vector field θ, we obtain the desired shape derivative (29). Since $\Gamma_{N_{\text{cut}}} \subset \Gamma_D$ and θ vanishes on Γ_D, the integral on $\Gamma_{N_{\text{cut}}}$ in the Lagrangian (30) does not contribute to the shape derivative. $\qquad\square$

6.2 Numerical test case for the baseplate separation problem

A new test case is considered here to highlight the criterion (25). It is a problem of arch design: for its final use the boundary conditions are shown on Figure 14. The computational domain D is a box $[0, 90mm] \times [0, 30mm] \times [0, 9mm]$, discretized with 56000 nodes and corresponding to half of the domain showed in Figure 14 (a symmetry condition is used). The mechanical properties are $E = 125$ GPa and $\nu = 0.26$. The force $f = (0, 0, -0.5)$ is applied on a $6mm^2$ square area centered on the bottom boundary of the domain. The Dirichlet boundary Γ_{D_f} is located on the tips of the bottom boundary, on two $2.5mm^2$ bands. The inherent strain tensor used for our simulation is again (4).

A reference shape ω_{ref} is obtained by minimizing the compliance (7) with a volume constraint $|\omega_{\mathrm{ref}}| = 0.33|D|$. It is displayed on Figure 15. We then solve (25) with $M = 20$ macro-layers.
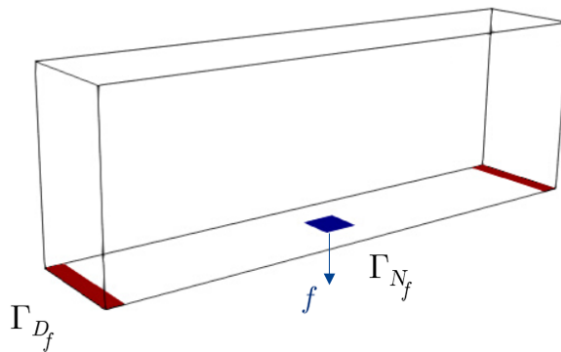

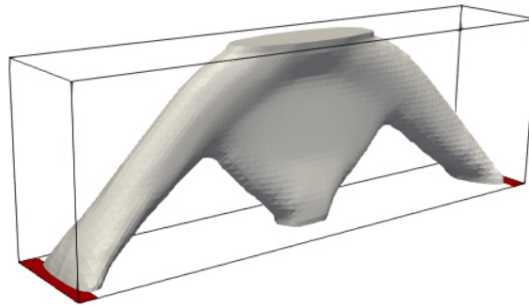Figure 14: Boundary conditions and loads for the arch problem.

Figure 15: Reference shape obtained by compliance minimization for the arch problem.

The boundary conditions for the separation model (24) are shown on Figure 16. The boundary $\Gamma_{D_{\mathrm{cut}}}$ (in red) models the non-cut part of the baseplate and is applied on a $270mm^2$ area on the bottom border. Note that our choice of $\Gamma_{D_{\mathrm{cut}}}$ is arbitrary. In truth, one should consider various lengths for $\Gamma_{D_{\mathrm{cut}}}$, modeling the different steps of the separation process. Here, $\Gamma_{D_{\mathrm{cut}}}$ is sufficiuently large so that the cut part is still attached to the baseplate in order to measure experimentally its deflection in Section 7.

The optimized shape solution of problem (25) is shown on Figure 17 (right). A small bar appears to connect the cut part of the shape to the baseplate in order to reduce the deflection. The numerical deflections for the initial and optimized geometries shown on Figure 18 confirm this intuition. The convergence history curves are plotted on Figure 19. This optimization took 500 iterations and the computational time was 30 hours.
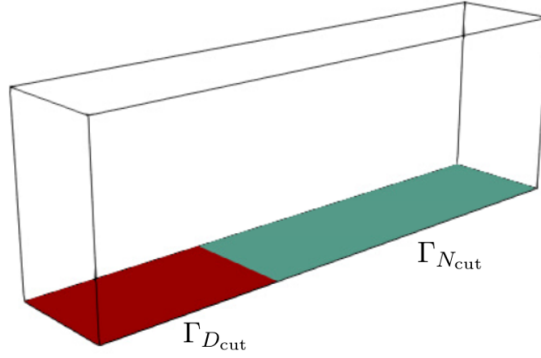
Figure 16: Boundary conditions on the baseplate for the separation model (24).

Figure 17: Initial geometry (left) and optimized (right) for minimizing (25) after the partial cut.
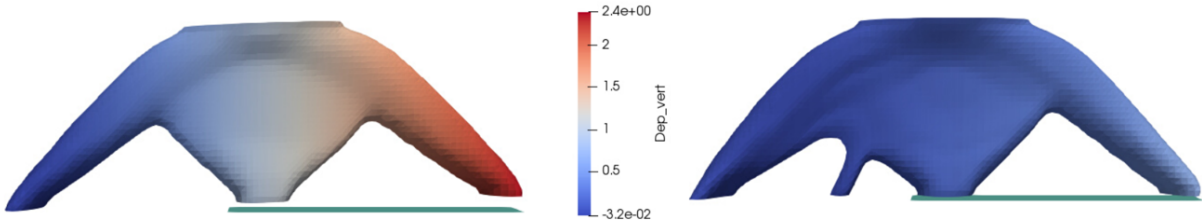

Figure 18: Vertical deflection of the initial geometry (left) and optimized (right).

Remark 6.2. *The same test case, namely solving (25) with the criterion (26), was performed for a MBB beam. The resulting vertical displacements, after baseplate separation, are plotted on Figure 20 for the reference MBB beam (left) and for the optimized design (right). For its final use the MBB beam has to resist a 3-point bending which is close, in practice, to the effect of a stress release during the cutting step from the baseplate. The deflection of the reference design is therefore already very small and it is hard to measure (less than 1mm) and, even more, to observe a significative difference between the reference and optimized MBB beams. This explains why we considered the arch design, for which the differences can be experimentally measured, as we shall see in the next section.*

7   Experimental assessment and calibration

The inherent strain model used in this work delivers at best the tendencies of the part behaviour during its manufacturing. To confirm its validity, an experimental study was performed by manufacturing in SLM two geometries: the MBB beam and the arch test case of Subsection 6.2. A picture of the built shapes on the baseplate after powder removal
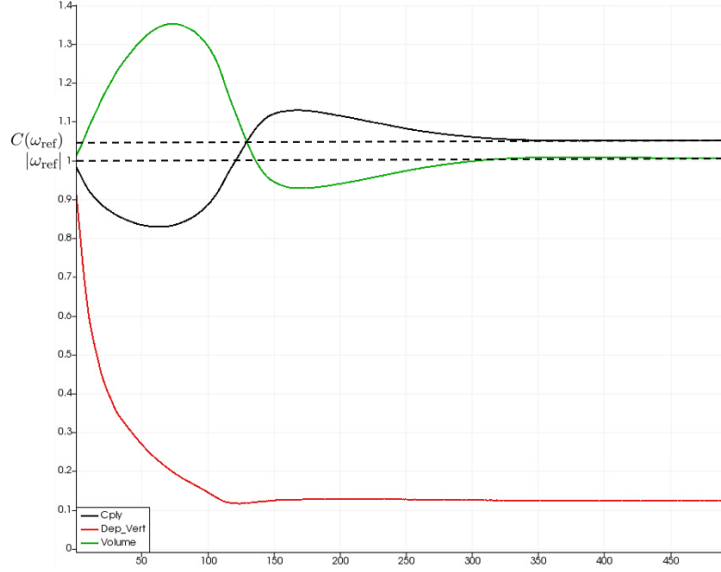
Figure 19: Convergence history for the arch design: criterion $J_3(\omega)$ (in red), compliance $C(\omega)$ (in black) and volume $|\omega|$ (in green).
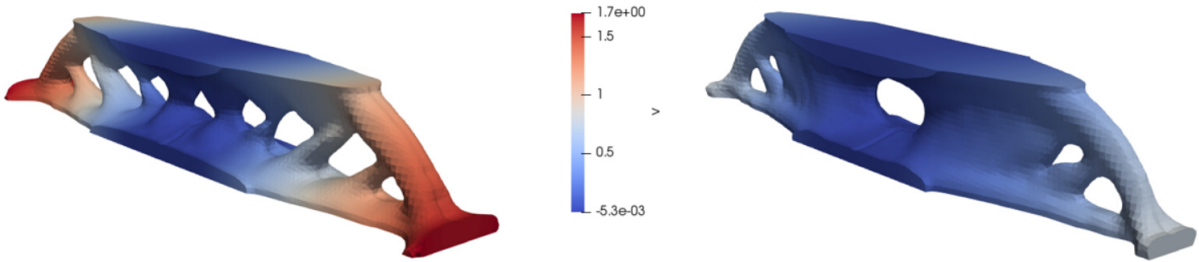

Figure 20: Reference MBB beam (left) and optimized MBB beam (right) for the vertical displacement criterion (26) after partial cut from the baseplate.

is shown on Figure 21. The experiment involves 15 parts: 6 arches and 9 MBB beams. For the arches, 3 are reference designs, simply optimized for the final-use compliance, and 3 are optimized designs for the vertical displacement criterion (26) after the baseplate separation (corresponding to Figure 17, left and right, respectively). For the MBB beams, 3 are reference designs, simply optimized for the final-use compliance (see Figure 7), 3 are optimized designs for the vertical displacement criterion (17) (see Figure 8) and 3 are optimized for the criterion (26) (see Remark 6.2 and [11] for further details). The 3 reference designs and the 3 optimized ones for (17) are shown in Figure 22. For every design, 3 parts are manufactured with exactly the same geometry in order to average the results which may vary depending on where the parts are placed on the baseplate. The fabrication, with Ta6V, was made by SafranTech, the research center of Safran group. It took 10 hours considering a thickness layer of 50 μm. A band scanning strategy was used: the powder bed was scanned with parallel lines by the laser beam. A 67° rotation in the direction of the trajectories was done between each layer to homogenize the strains in the horizontal layer plane.
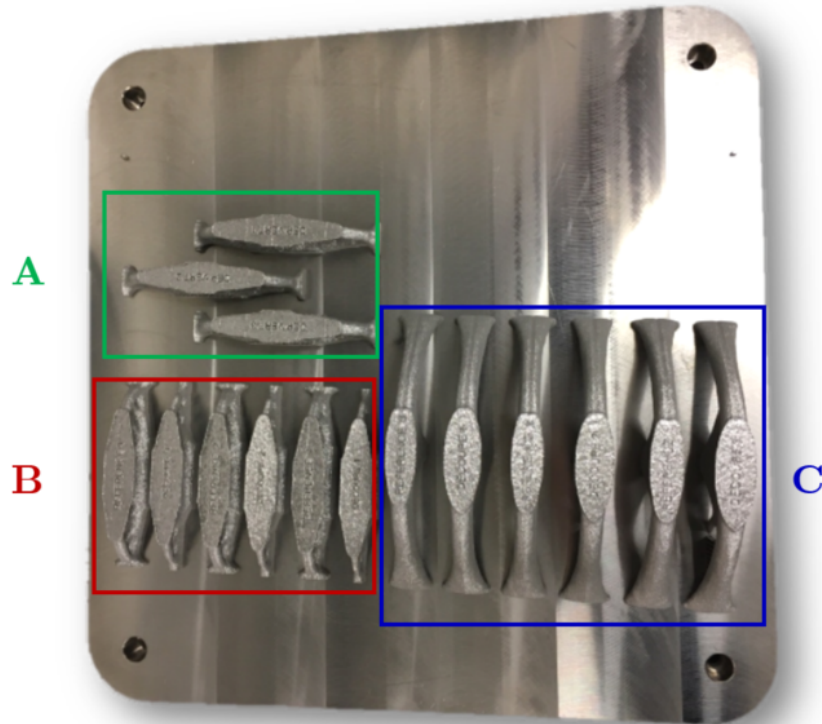
21

Figure 21: Fabrication after powder removal comprising 15 geometries. In the green frame (A) are the optimized MBB beams for (17) and in the red frame (B) are the reference MBB beams ; in the blue frame (C) are the reference and optimized arches for (26).

7.1 Displacement measurements after partial cut from the baseplate

This subsection is concerned with the 6 arches on the right hand side of the baseplate (blue frame (C) on Figure 21): 3 of them are reference geometries (left of Figure 17) and the 3 others are the optimized geometries (right of Figure 17) for the criterion (26). Another view of the optimized arch is shown on Figure 23 where one can see a thin support, added between two vertical bars to ensure the manufacturing of the overhang surface. This support (0.1 mm thin) was created with the software *Magics Materialise®*[2] and it was removed by hand just after the depowdering step, so it does not impact the part behaviour during its partial cut from the baseplate. After removing this support, the six arches have been partly separated from the baseplate in one operation by EDM (Electrical Discharge Machining). A picture of these arches is shown in Figure 24 where one can see a clear deflection difference between the reference and the optimized arches (as expected from the numerical results).

To precisely measure this deviation, the baseplate and the arches are scanned before and after the cutting process. The result of these two scans are shown in Figure 25. The overlay of the two scans is made with the *GOM Inspect* ®software [3] and highlights the difference of position at each point, as shown in Figure 26. The vertical position at the tip of each part is then measured for both scans. The average vertical displacement at the

---

[2]https://www.materialise.com
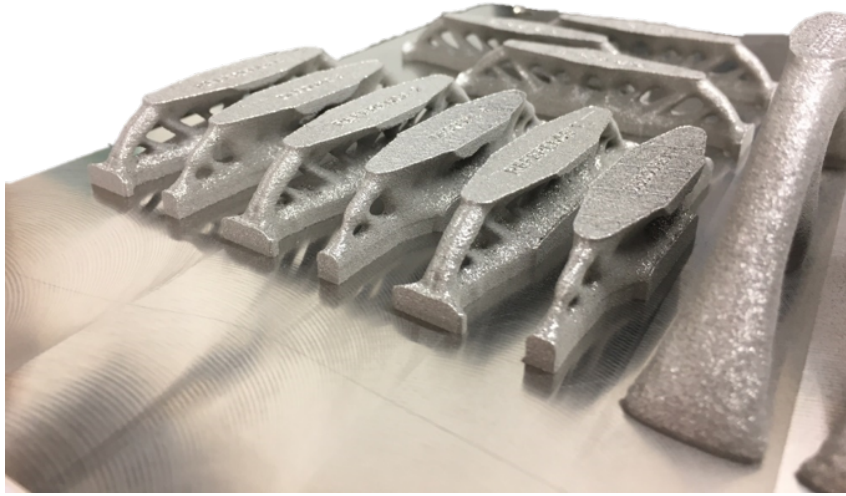[3]https://www.gom-inspect.com

Figure 22: Reference and optimized MBB beams for the criterion (17).
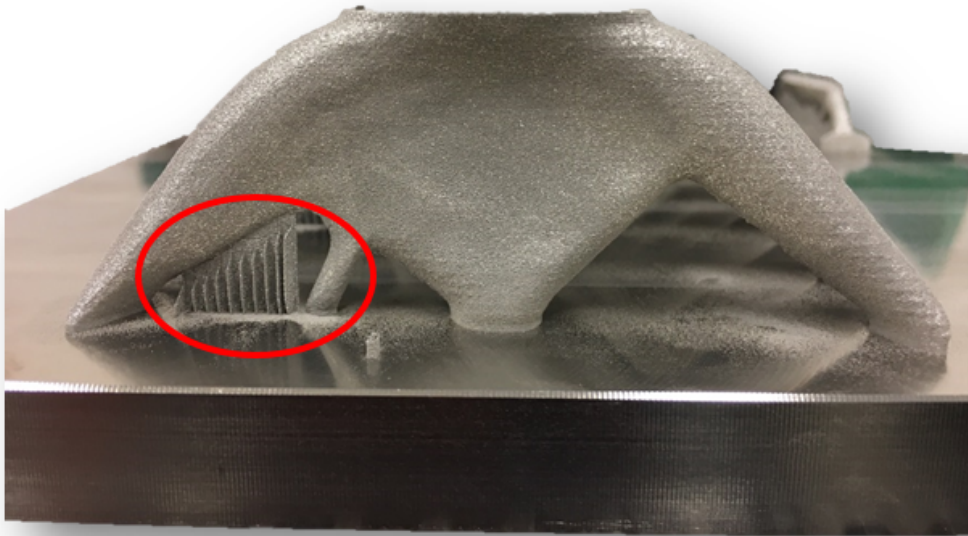
Figure 23: Optimized arch for the criterion (26) manufactured with a thin support (circle in red) to ensure the construction of the overhang surface.

tip of the reference design is 2.31 mm and 1.23 mm for the optimized one. So an average reduction of 47% is observed for an equivalent volume between the two designs.

7.2 Observation of the powder bed at each layer

As already said overhang and non-supported surfaces may deform resulting in a poor surface quality or a stop of the machine. To avoid this effect, the vertical displacement

Figure 24: Partially cut arches. A difference in deflection can be observed between the reference and optimized arches.
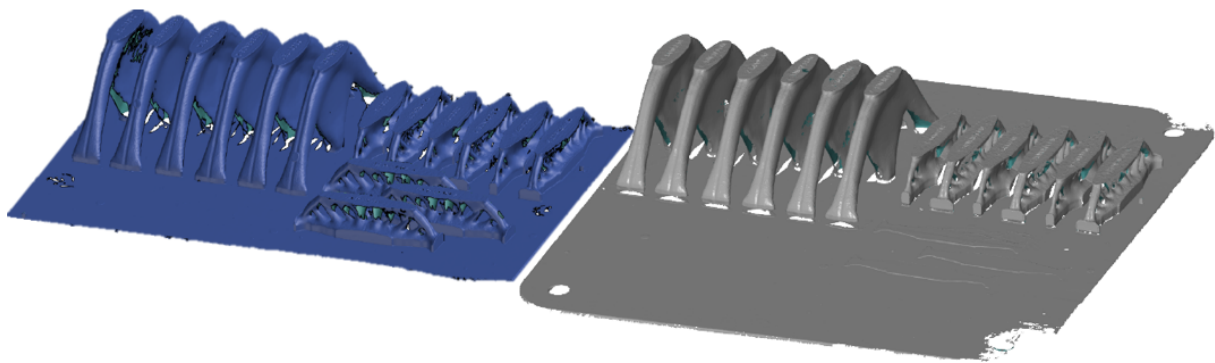
Figure 25: Scans of the baseplate before the partial cut step (left) and after (right).
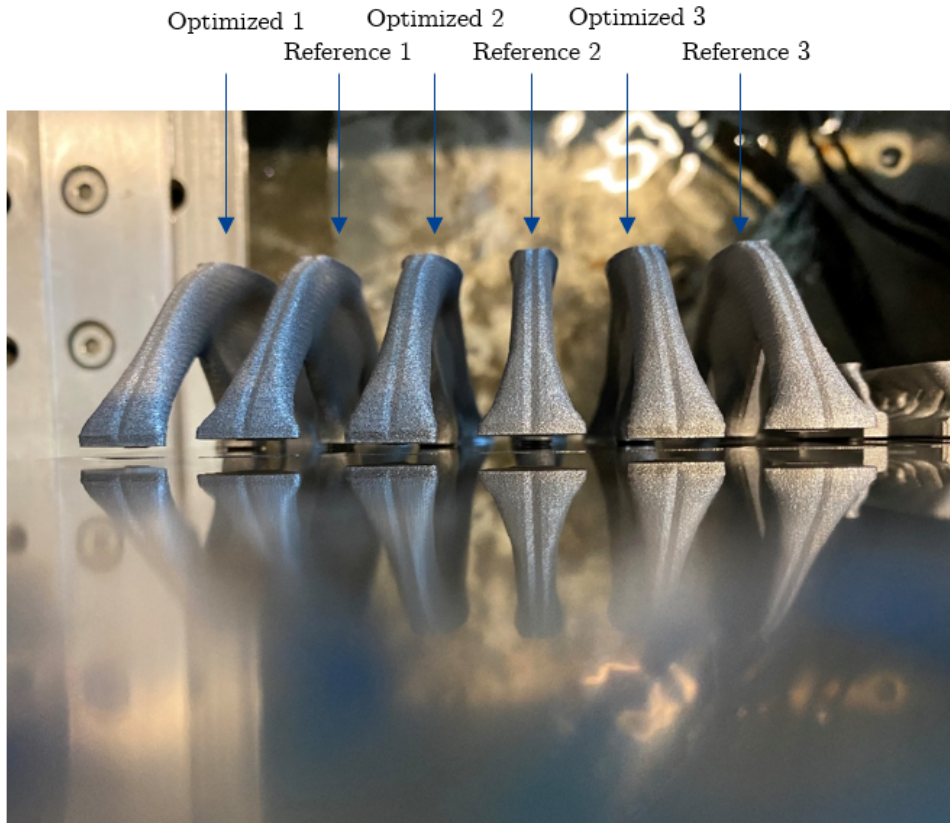
criterion (17) was formulated and minimized. We now provide pictures of the powder bed, taken before and after each recoating step, to support the claim that overhang surfaces can stop the machine. These pictures allow us to detect a posteriori some possible manufacturing problems, especially when some layers exceed the powder bed of the next layer. This phenomenon is observed at the 214th layer where the powder bed is shown in Figure 27, before and after the recoating step. The tips of the non-supported layers of the reference geometries are visible on the right of Figure 27 (red circle). The recoater hit indeed these parts and almost deteriorated them. However, the powder bed is clean at the places where the optimized geometries (for the criterion (17)) are manufactured. This is a clear experimental validation that our optimized designs have smaller deformations

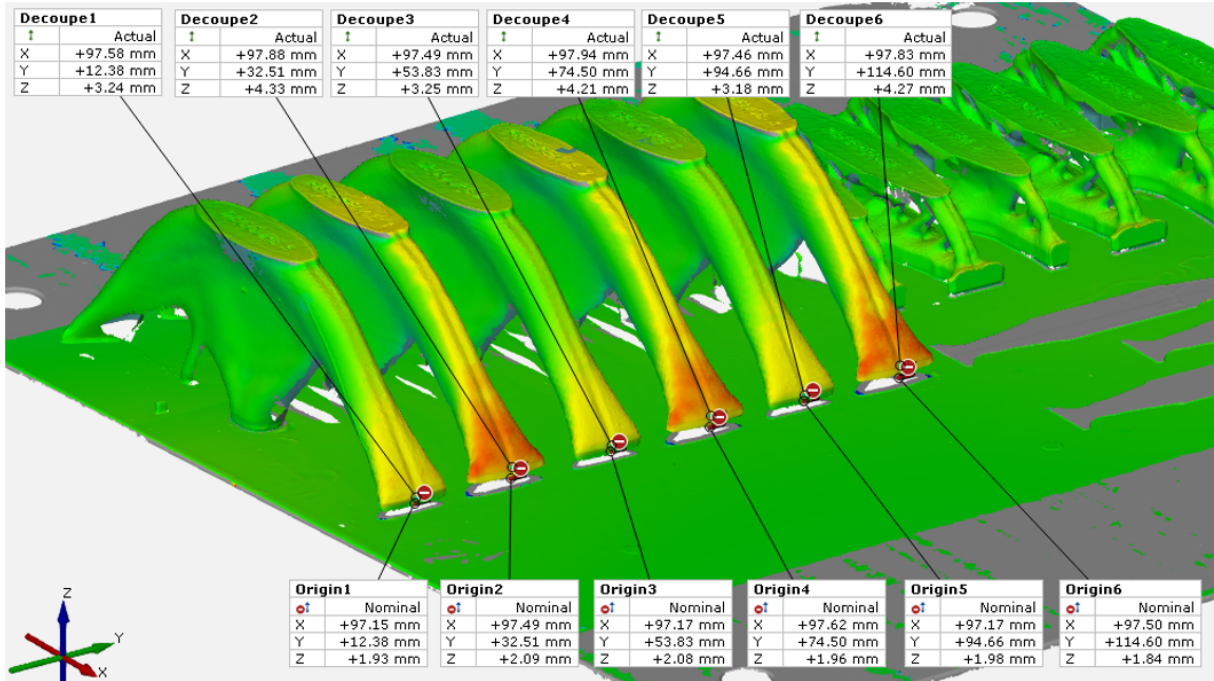| Decoupe1		Decoupe2		Decoupe3		Decoupe4		Decoupe5		Decoupe6	
‡	Actual	‡	Actual	‡	Actual	‡	Actual	‡	Actual	‡	Actual
X	+97.58 mm	X	+97.88 mm	X	+97.49 mm	X	+97.94 mm	X	+97.46 mm	X	+97.83 mm
Y	+12.38 mm	Y	+32.51 mm	Y	+53.83 mm	Y	+74.50 mm	Y	+94.66 mm	Y	+114.60 mm
Z	+3.24 mm	Z	+4.33 mm	Z	+3.25 mm	Z	+4.21 mm	Z	+3.18 mm	Z	+4.27 mm

Origin1		Origin2		Origin3		Origin4		Origin5		Origin6	
o‡	Nominal	o‡	Nominal	o‡	Nominal	o‡	Nominal	o‡	Nominal	o‡	Nominal
X	+97.15 mm	X	+97.49 mm	X	+97.17 mm	X	+97.62 mm	X	+97.17 mm	X	+97.50 mm
Y	+12.38 mm	Y	+32.51 mm	Y	+53.83 mm	Y	+74.50 mm	Y	+94.66 mm	Y	+114.60 mm
Z	+1.93 mm	Z	+2.09 mm	Z	+2.08 mm	Z	+1.96 mm	Z	+1.98 mm	Z	+1.84 mm

Figure 26: Overlay of the two baseplate scans.

during the layer-by-layer building process.

7.3 Inverse analysis for the inherent strain calibration

In this subsection we show how the inherent strain tensor ϵ^* can be recovered by an inverse analysis based on the experimental results of the previous subsection. The measured elastic springback on the manufactured parts are used as data for an inverse analysis enabling to find numerically the entries of the inherent strain tensor ϵ^* of the direct problem (3). We choose to have two optimization parameters $a_1, a_2 \in \mathbb{R}$, which are
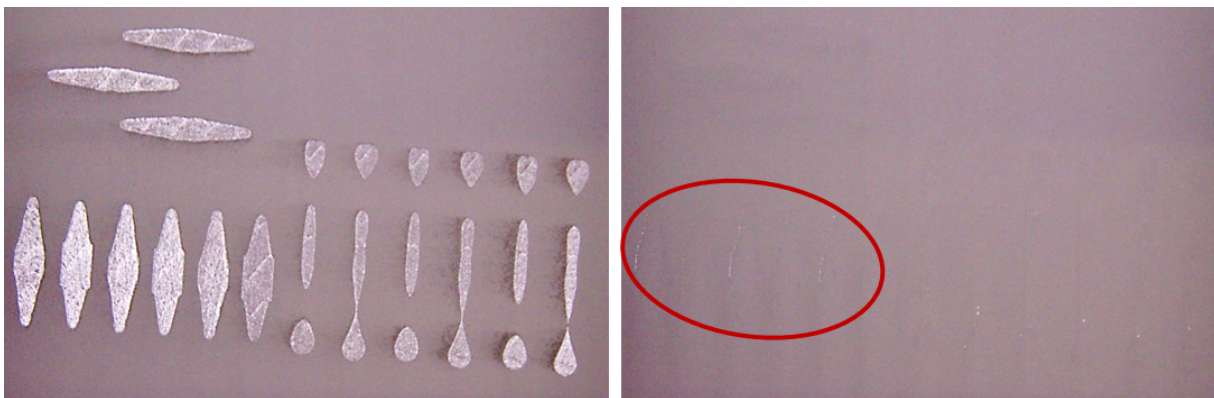

Figure 27: Picture of the powder bed of the 214th layer after scanning (left) and of de 215th before scanning (right). Some of the layer tips previously fused have been deformed above the powder bed (inside the red circle).

gathered in a 3×3 diagonal matrix defined by

$$\epsilon^*(a) = \begin{pmatrix} -a_1 10^{-4} & 0 & 0 \\ 0 & -a_2 10^{-4} & 0 \\ 0 & 0 & 0 \end{pmatrix}. \tag{31}$$

The third diagonal coefficient is null as the inherent strains are assumed to be restricted to the plane layer. The value of $\epsilon^*(a)$ is used for ϵ^* in the inherent strain problem (3).

The goal of the inverse problem is to find the values of a_1, a_2 which imply that the solution of (3) matches the measured data. In other words, the goal is to minimize a least square function quantifying the deviations of the model from the measures:

$$J_{\text{inv}}(a) = \int_\omega j_{\text{inv}}(v) \, dx, \tag{32}$$

where v is the solution of (24) and

$$j_{\text{inv}}(v) = \int_\omega \sum_{i=1}^{N_{\text{msr}}} |\bar{v}_z(x_i) - v_z(x)|^2 \chi_{\mathcal{B}_\varepsilon(x_i)}, \tag{33}$$

where N_{msr} is the number of measured points on the part, $\bar{v}_z(x_i)$ the vertical displacement measured at the point x_i, $v_z(x)$ the vertical displacement computed with the model (3), considering the inherent strain tensor $\epsilon^*(a)$, and $\chi_{\mathcal{B}_\varepsilon(x)}$ is the characteristic function associated to the ball $\mathcal{B}_\varepsilon(x)$ of radius ε centered on the point x. In practice, ε is the size of a mesh cell.

To solve this unconstrained optimization problem, the BFGS algorithm (see chapter 6 in [28]) is used, which requires to evaluated the derivative of J_{inv} with respect to the variable a. For that purpose, two adjoint problems, similar to (9) and (27), are introduced. The first adjoint problem, associated to (24) is written

$$\begin{cases} -\text{div}(Ae(\eta)) &=& -j'_{\text{inv}}(v) & \text{in } \omega, \\ Ae(\eta)n &=& 0 & \text{on } \Gamma_{N_{\text{cut}}} \\ \eta &=& 0 & \text{on } \Gamma_{D_{\text{cut}}} \end{cases} \tag{34}$$

with

$$j'_{\text{inv}}(v) = 2 \sum_{i=1}^{N_{\text{msr}}} (\bar{v}_z(x_i) - v_z(x))\chi_{\mathcal{B}_\varepsilon}(x_i).$$

The second adjoint problem is the same as (28).

Lemma 7.1. *The gradient of J_{inv} with respect to $a \in \mathbb{R}^2$ is, for any $\delta a \in \mathbb{R}^2$,*

$$\nabla_a J_{inv} \cdot \delta a = \sum_{i=1}^M \int_{\omega_i} A(\epsilon^*(\delta a)\chi_{\mathcal{L}_i}) : e(p_i) \, dx. \tag{35}$$

Proof. The new Lagrangian is written as:

$$\mathcal{L}(a, \hat{v}, \hat{\eta}, \{\hat{u}_i\}, \{\hat{p}_i\}) = \int_\Omega j_{\text{inv}}(\hat{v})dx + \int_\omega \left(Ae(\hat{v}) + \sum_{j=1}^M Ae(\hat{u}_j) \right) : e(\hat{\eta}) \, dx$$

$$- \int_{\Gamma_{N_{\text{cut}}}} \sum_{j=1}^M Ae(\hat{u}_j)n \cdot \hat{\eta} \, ds \tag{36}$$

$$+ \sum_{i=1}^M \int_{\omega_i} A(e(\hat{u}_i) + \epsilon^*(a)\chi_{\mathcal{L}_i}) : e(\hat{p}_i) \, dx.$$

Differentiating $\mathcal{L}$ with respect to $\hat{v}, \hat{\eta}_j, \{\hat{u}_i\}, \{\hat{p}_i\}$, the different variationnal formula of (27), (24), (9), and (3) are obtained respectively. Finally, (35) is obtained by differentiating $\mathcal{L}$ with respect to a. $\qquad\square$

7.4   Matching of synthetic data

A numerical test with synthetic data is first considered to evaluate the method. A well-known geometry, called "comb", is used. It is shown in Figure 28 (left) in a domain of size $[0, 72mm] \times [0, 10mm] \times [0, 6mm]$, discretized using 5621 nodes.

A symmetry with respect to the XZ plane is used to reduce the size of the computational domain. Problem (3) is first solved using $a_{1,\text{ref}} = a_{2,\text{ref}} = 0.5$ to yield synthetic data $\bar{v}_z(x_i)$. The mechanical properties are $E = 125$ GPa, $\nu = 0.3$ and the domain is divided in $M = 10$ horizontal layers. As shown in Figure 28 (right), $N_{\text{msr}} = 19$ points x_i aligned on the top face of the comb are considered. Their coordinates along the x axis are reported in Table 1. In order to test the robustness of the model, some noise is applied to the synthetic data $\bar{v}_z(x_i)$. A random deviation of 2% is added to each value $\bar{v}_z(x_i)$. These perturbed values are reported in Table 1.
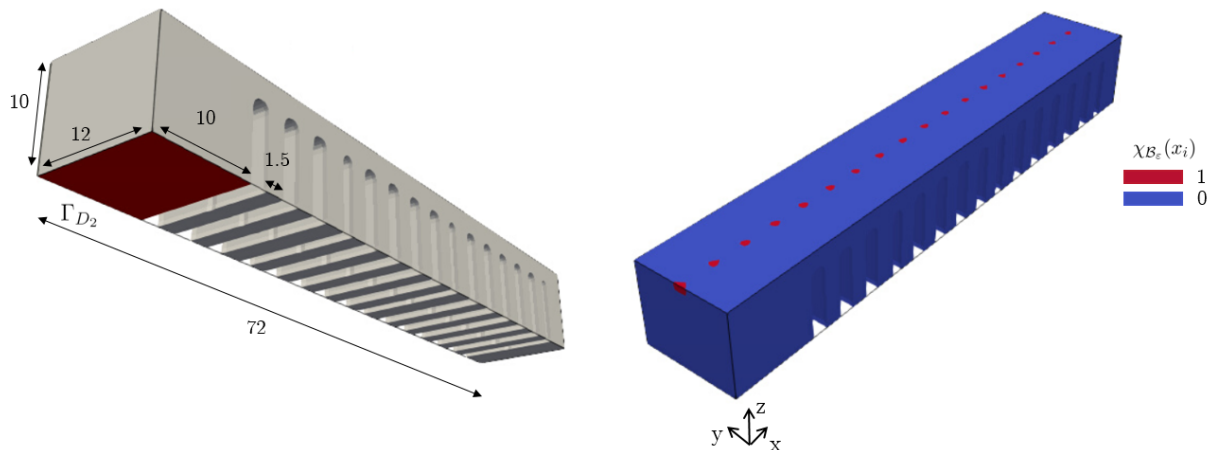

Figure 28: "Comb" geometry (left) and characteristic functions $\chi_{\mathcal{B}_\varepsilon}(x_i)$ of the least square criterion (right).

Then, (33) is minimized with respect to the variables a_1 et a_2, in order to match the vertical displacementst $v_z(x_i)$ with the noised synthetic data $\bar{v}_z(x_i)$, previously obtained with $a_{1,\text{ref}}$ and $a_{2,\text{ref}}$. The optimization variables are initialized with $a_1 = a_2 = 0.1$ for a cost functional $J_{\text{inv}}(a) = 74273$. Convergence is reached after 14 iterations and the optimized variables are $a_1 = 0.47$ and $a_2 = 0.54$ (not very far from the true values $a_{1,\text{ref}} = a_{2,\text{ref}} = 0.5$) for a cost $J_{\text{inv}}(a) = 0.42$. The values of the vertical displacements for the optimized variables are reported in Table 1. The vertical displacements $v_z(x_i)$ are close to the noised data $\bar{v}_z(x_i)$, which gives confidence that the same algorithm can be used with experimental data.

7.5   Matching of experimental data

We now use experimental values measured at $N_{\text{msr}} = 10$ points x_i, distributed on the edge of the most deformed bar and shown on Figure 29. The values of their vertical

points	position $x(mm)$	$\bar{v}_z(x_i)(mm)$	$v_z(x_i)(mm)$
x_1	720	9.81	9.81
x_2	680	8.99	9.98
x_3	640	8.17	8.16
x_4	600	7.35	7.34
x_5	560	6.54	6.53
x_6	520	5.74	4.74
x_7	480	4.96	4.96
x_8	440	4.22	4.21
x_9	400	3.47	3.47
x_{10}	360	2.79	2.78
x_{11}	320	2.15	2.14
x_{12}	280	1.58	1.57
x_{13}	240	1.08	1.08
x_{14}	200	0.65	0.63
x_{15}	160	0.30	0.29
x_{16}	120	0.09	0.07
x_{17}	80	0.01	0.01
x_{18}	40	0.00	00
x_{19}	0	0.00	00

Table 1: Position on the x axis and vertical displacement computed on the point x_i for the coefficient $a_{1,\text{ref}}$ and $a_{2,\text{ref}}$, and computed with the coefficient obtained after at convergence.

displacements, after the partial cut, are reported in Table 2. The associated characteristic functions $\chi_{\mathcal{B}_\varepsilon}(x_i)$ are plotted on the geometry, in Figure 30.

Remark 7.2. *For practical reasons, the dimensions of the manufactured arch, as well as the numerical model of the same arch, are slightly larger than the ones considered numerically (scaling by a factor 1.18 in each dimension). This has no influence on the inverse analysis of the present subsection.*

As said before, the band scanning strategy has been used to manufacture the parts. The periodic nature of this strategy leads to study an isotropic application of the inherent strain in the plane layer. With this new assumption, only one parameter needs to be considered since it is assumed that $a_1 = a_2$. The optimization parameter is initialized by $a_1 = 1$. Convergence is reached after 20 iterations with $a_1 = 0.5359$. The final value of the objective function is $J_{\text{inv}}(a) = 0.367$. The convergence history curves are shown in Figure 31.

The vertical displacements $v_z(x_i)$ computed with $a_1 = a_2 = 0.5359$ are reported in the Table 2 as well as the coordinates of the points x_i in the median plane with respect to the left tip of the part (see the coordinate system in Figure 30).

Remark 7.3. *One of the main difficulties was to match the numerical coordinates of the point x_i with the physical ones. Those are determined with respect to the coordinates system located at the left tip of the part and placed in the same way in the FreeFEM software. However, the measures made by hand with GOM Inspect® are accurate to the hundredth of a millimeter, so a slight variation of position would have a significant impact on the function $J_{inv}(a)$ as well as on the optimization result.*
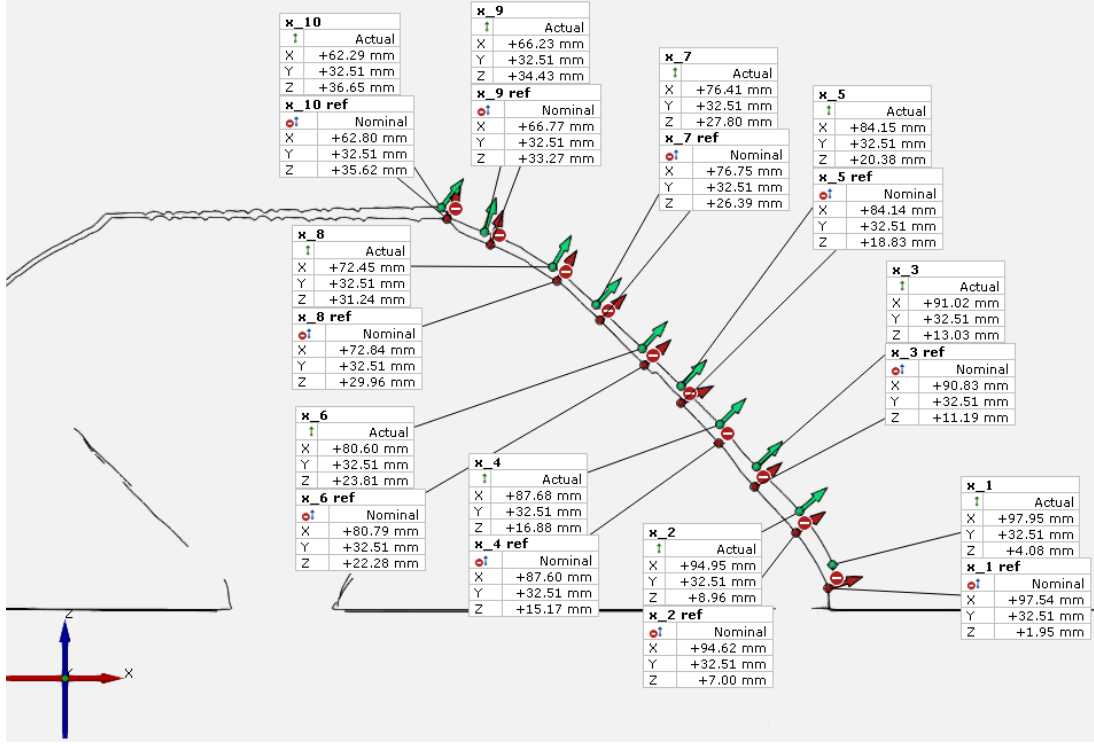
Figure 29: Median planes of the manufactured shape ω_{ref}, before and after baseplate separation on which the measures $\bar{v}_z(x_i)$ are taken.
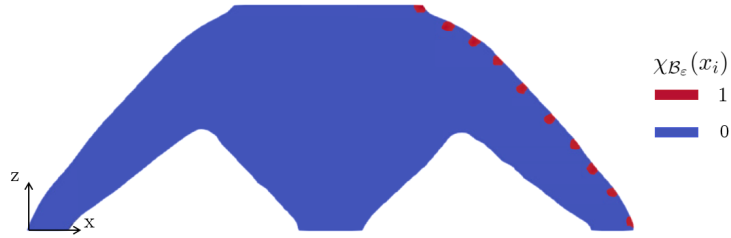

Figure 30: Characteristic functions $\chi_{\mathcal{B}_\varepsilon}(x_i)$ of the least square criterion.

The comparison of the values $\bar{v}_z(x_i)$ and $v_z(x_i)$ in Table 2 is quite satisfactory in view of the simplicity of the simulation model and the difficulty to take accurate measures on the part. In a future work, it would be interesting to validate the model with other geometries. Moreover, the scanning strategy used for this experiment allows us to make implifying assumptions for the inverse analysis. More studies are required to find $\epsilon^*_{\mathcal{L}_i}$ when another scanning strategy is used to manufacture the part. In addition, physical guides have to be designed during the baseplate preparation in order to facilitate the measurement.

8 Optimization of support structures

In this section, the built part ω is assumed to be fixed and only its supports S are subject to optimization. Support structures are required to ensure an efficient manufacturability of the part when it cannot be modified. Supports are some extra material connecting further the part to the baseplate, and their role is to minimize the deformations induced
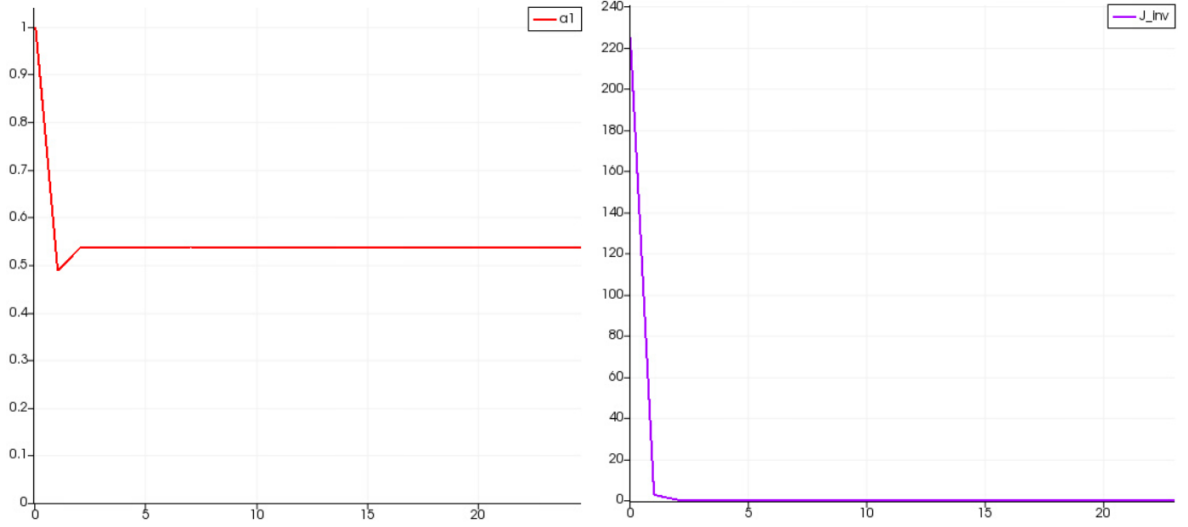
Figure 31: Convergence history curves for a_1 (left) and for $J_{\text{inv}}(a)$ (right).

points	position $x(mm)$	position $z(mm)$	$\bar{v}_z(x_i)(mm)$	$v_z(x_i)(mm)$
x_1	97,7	1.1	2.13	1.98
x_2	95.5	4.7	1.96	1.92
x_3	93.3	8.3	1.84	1.86
x_4	88.8	14.2	1.71	1.74
x_5	84.4	17.8	1.58	1.62
x_6	80.9	22.3	1.53	1.53
x_7	76.6	27.2	1.41	1.42
x_8	72.7	30.2	1.28	1.34
x_9	66.6	33.4	1.16	1.19
x_{10}	62.2	35.6	1.05	1.09

Table 2: Position of the point x_i and the associated vertical displacements $\hat{v}_z(x_i)$ measured. $v_z(x_i)$ is the vertical displacement computed with our model with the inherent strain tensor $\epsilon^*_{\mathcal{L}_i}$ obtain by inverse analysis.

by the process. We denote by Ω the supported structure composed of the part ω and its supports S,

$$\Omega = \omega \cup S.$$

The supported structure Ω is divided into M layers, and each intermediate shape is built from the first i layers such that $\Omega_i = \Omega \cap D_i$. Compared to (3), the manufacturing problem is now solved in the supported structure Ω, instead of just ω. Therefore, (3) is rewritten as

$$\begin{cases} -\text{div}(\sigma_i) &= 0 & \text{in } \Omega_i, \\ \sigma_i &= A\left(e(u_i) + \epsilon^*_{\mathcal{L}_i}\right) & \text{with } \epsilon^*_{\mathcal{L}_i}(x) = \epsilon^* \chi_{\mathcal{L}_i}(x), \\ \sigma_i n &= 0 & \text{on } \Gamma_{N_i}, \\ u_i &= 0 & \text{on } \Gamma_D \cap \partial\Omega_i. \end{cases}$$

We consider again the criterion (17), which is the sum of contributions from each intermediate structure Ω_i, depending on their vertical displacements, namely

$$J_4(S) = \sum_{i=1}^{M} \int_{\Omega_i} j_4(u_i)dx \quad \text{with} \quad j_4(u_i) = |\max(0, u_i \cdot e_d)|^2 \chi_{\mathcal{L}_i}. \tag{37}$$

The only difference with (17) is that the criterion is now integrated on Ω_i instead of ω_i.

Since the part ω is fixed, the performance of the shape for its final use is not considered, so the optimization problem becomes

$$\begin{aligned} \min_{S \subset D \setminus \omega} \quad & J_4(S) \\ \text{s.t.} \quad |S| \quad & = \quad |S_{\text{init}}|, \end{aligned} \tag{38}$$

where $|S|$ is the volume of the support structure and $|S_{\text{init}}|$ is the volume of the initial support structure. The boundary $\partial S = \partial S_D \cup \partial S_0 \cup \partial S_\omega$ is decomposed in three disjoint subsets: ∂S_D is the boundary of S attached to the baseplate, ∂S_0 is the boundary of S free to move and ∂S_ω is in contact with the fixed shape ω. We denote by n_S and n_ω the unit normal vectors to S and ω, respectively.

Assumption 8.1. *Since the support cannot penetrate in the part ω (which is fixed), the displacement fields $\theta \in W^{1,\infty}(D, \mathbb{R}^n)$ are restricted by the condition $\theta \cdot n_\omega = 0$ on $\partial S_\omega = \partial S \cap \partial \omega$. Note that ∂S_ω can move tangentially on $\partial \omega$. Of course, the baseplate is fixed and θ is thus assumed to vanish on Γ_D.*

Proposition 8.2. *Under Assumption 8.1, the shape derivative of $J_4(S)$ in the direction of the vector field θ is given by*

$$J_4'(S)(\theta) = \sum_{i=1}^{M} \int_{\partial S_0 \cap D_i} \theta \cdot n \Big(j_4(u_i) + A\left(e(u_i) + \epsilon_{\mathcal{L}_i}^*\right) : e(p_i) \Big) ds, \tag{39}$$

Proof. The proof is very similar to that of Proposition 3.2. Introducing the Lagrangian

$$\mathcal{L}(\Omega, \{u_i\}, \{p_i\}) = \sum_{i=1}^{M} \int_{\Omega_i} j_4(u_i) \, dx + \sum_{i=1}^{M} \int_{\Omega_i} A\left(e(u_i) + \epsilon_{\mathcal{L}_i}^*\right) : e(p_i) \, dx$$

and differentiating $\mathcal{L}$ with respect to all the variables give the desired result (39). $\qquad \square$

We now define a test case for the optimization problem (38). The computational domain D is a box $[0, 80mm] \times [0, 100mm] \times [0, 80mm]$, discretized with 48000 nodes and corresponding to a quarter of the domain shown in Figure 32 (two symmetry conditions are used). The mechanical parameters are $E = 125$ GPa and $\nu = 0.26$ for both subdomains ω and S. As usual, the baseplate Γ_D is the bottom boundary. The inherent strain tensor ϵ^* is again (4). The fixed part ω, to be built, is displayed on Figure 32 (it was obtained by another compliance minimization problem). Solving the inherent strain model (3) in ω without any supports yield vertical displacements displayed on the right of Figure 32. As expected, the magnitude of the vertical displacements is larger on the overhang surfaces when the part is manufactured without any supports.

The support initialization (in blue) for optimizing (38) is displayed on Figure 33 (left). The optimized supports (in blue) is shown on Figure 33 (right): they cover the whole overhang area of the part ω (in red) and do not feature any overhang surface by themselves. It is striking that the sole criterion (37) allows us to eliminate all overhang surfaces for the complete structure Ω. Convergence histories are plotted in Figure 34.
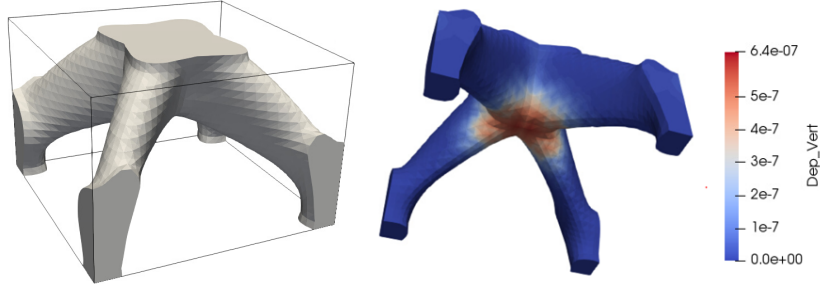
Figure 32: Fixed part ω to build (left) and associated vertical displacements predicted by the inherent strain model (right).
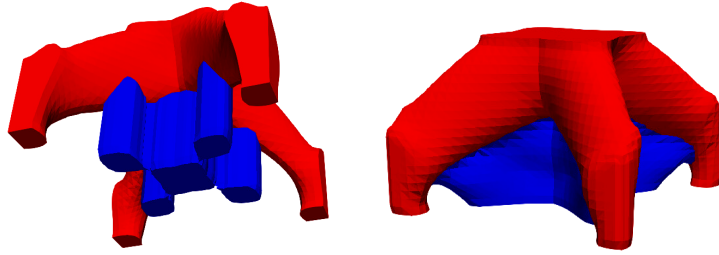

Figure 33: Supports S in blue: initial ones (left) and optimized ones (right) for the fixed part ω in red.
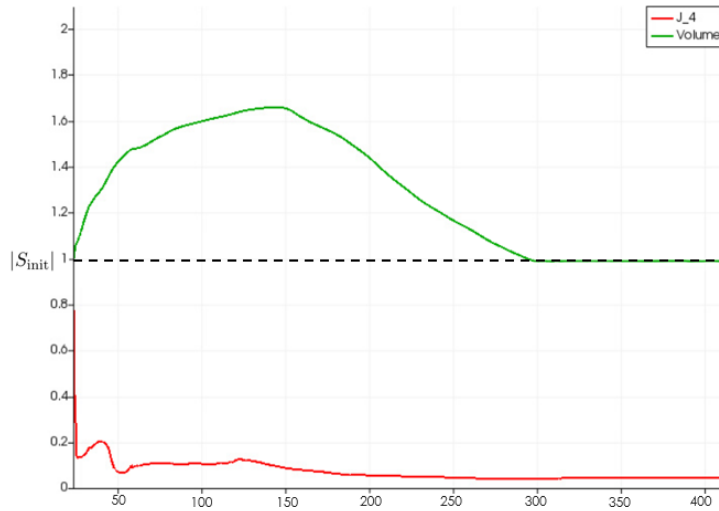

Figure 34: Convergence history for the objective function $J_4(\Omega)$ (red) and the volume $|S|$ (green).

9   Conclusions and perspectives

In this paper, several optimization criteria are proposed to minimize defects caused by the metal powder bed additive manufacturing process. These criteria are evaluated with a simple, yet efficient, process simulation based on the *inherent strain* model. This purely mechanical model is able to predict the displacements endured by the part during its manufacturing, with given process parameters. This process simulation was included in a shape and topology optimization framework in order to minimize the main manufacturing defect measures, such as vertical displacements or residual stresses. A criterion was also formulated for a post-manufacturing constraint, namely the deflection of the part after

baseplate separation. The numerical results have been assessed by manufacturing some optimized and reference geometries. These experimental results have also been used to performed an inverse analysis to calibrate the inherent strain model. Finally, support structure were optimized, with a criterion acting on vertical displacements in the fixed part and on the support structure itself.

Of course, it is possible to generalize our approach to the simultaneous optimization of the built part and its supports (at the price of an increased computational time). The inherent strain model used in this work has some flaws [14] and could be enriched if it is unable to reproduce some experimental results, for example by considering a non-homogeneous strain tensor or by adding plastic effects in the model. Other objective functions or criteria for detecting manufacturing defects could be proposed and studied. Finally, more realistic test cases and experiments are necessary for a complete assessment of our proposed shape and topology optimization approach.

References

[1] G. Allaire. *Conception optimale de structures*, volume 58 of Mathematiques & Applications. Berlin: Springer, 2007.

[2] G. Allaire, M. Bihr, and B. Bogosel. Support optimization in additive manufacturing for geometric and thermo-mechanical constraints. *Structural and Multidisciplinary Optimization*, 61:2377–2399, 2020.

[3] G. Allaire and B. Bogosel. Optimizing supports for additive manufacturing. *Structural and Multidisciplinary Optimization*, 58:2493–2515, 2018.

[4] G. Allaire, C. Dapogny, R. Estevez, A. Faure, and G. Michailidis. Structural optimization under overhang constraints imposed by additive manufacturing technologies. *Journal of Computational Physics*, 351:295–328, 2017.

[5] G. Allaire, C. Dapogny, A. Faure, and G. Michailidis. Optimisation de forme pour une contrainte mécanique associée aux procédés de fabrication additive. *C. R., Math., Acad. Sci. Paris*, 355(6):699–717, 2017.

[6] G. Allaire, C. Dapogny, and F. Jouve. Shape and topology optimization. *Handb. Numer. Anal.*, 22:1–132, 2021.

[7] G. Allaire and L. Jakabcin. Taking into account thermal residual stresses in topology optimization of structures built by additive manufacturing. *Mathematical Models and Methods in Applied Sciences*, 28:2313–2366, 07 2018.

[8] G. Allaire, F. Jouve, and A.-M. Toader. Structural optimization using sensitivity analysis and a level-set method. *Journal of Computational Physics*, 194(1):363–393, 2004.

[9] A. Bandyopadhyay and S. Bose. *Additive manufacturing.* CRC press, 2019.

[10] M. P. Bendsøe and O. Sigmund. *Topology Optimization.* Springer Berlin Heidelberg, 2004.

[11] M. Bihr. *Optimisation Topologique du couple pi'ece/support pour la fabrication additive m'etallique sur lit de poudre.* PhD thesis, Institut Polytechnique de Paris, 2021.

[12] M. Boissier, G. Allaire, and C. Tournier. Additive manufacturing scanning paths optimization using shape optimization tools. *Structural and Multidisciplinary Optimization,* 61:2437–2466, 2020.

[13] M. Bugatti and Q. Semeraro. Limitations of the inherent strain method in simulating powder bed fusion processes. *Additive Manufacturing,* 23:329 – 346, 2018.

[14] M. Bugatti and Q. Semeraro. Limitations of the inherent strain method in simulating powder bed fusion processes. *Additive Manufacturing,* 23:329–346, 2018.

[15] C. M. Bui, C. Dapogny, and P. J. Frey. An accurate anisotropic adaptation method for solving the level set advection equation. *International Journal for Numerical Methods in Fluids,* 70:899–922, 2012.

[16] J. Céa. Conception optimale ou identification de formes, calcul rapide de la dérivée directionnelle de la fonction coût. *ESAIM: Mathematical Modelling and Numerical Analysis,* 20(3):371–402, 1986.

[17] Q. Chen, X. Liang, D. Hayduke, J. Liu, L. Cheng, J. Oskin, R. Whitmore, and A. C. To. An inherent strain based multiscale modeling framework for simulating part-scale residual deformation for direct metal laser sintering. *Additive Manufacturing,* 28:406 – 418, 2019.

[18] I. Gibson, D. Rosen, B. Stucker, and M. Khorasani. *Additive manufacturing technologies,* volume 17. Springer, 2014.

[19] F. Hecht. New development in FreeFem++. *J. Numer. Math.,* 20(3-4):251–265, 2012.

[20] L. J. Kumar and C. G. Krishnadas Nair. *Current Trends of Additive Manufacturing in the Aerospace Industry,* pages 39–54. Springer Singapore, Singapore, 2017.

[21] M. Langelaar. Topology optimization of 3d self supporting structures for additive manufacturing. *Additive Manufacturing,* 12:60–70, 2016.

[22] M. Langelaar. Integrated component-support topology optimization for additive manufacturing with post-machining. *Rapid Prototyping Journal,* 25:255–265, 2019.

[23] K. Manish and R. Gregory. *Design for metal additive manufacturing for aerospace applications,* pages 67–86. Elsevier, 2019.

[24] P. Mercelis and J. Kruth. Residual stresses in selective laser sintering and selective laser melting. *Rapid Prototyping Journal,* 12(5):254–265, 2006.

[25] L. Mugwagwa, D. Dimitrov, S. Matope, and I. Yadroitsev. Influence of process parameters on residual stress related distortions in selective laser melting. *Procedia Manufacturing*, 21:92–99, 2018.

[26] L. Mugwagwa, I. Yadroitsev, and S. Matope. Effect of process parameters on residual stresses, distortions, and porosity in selective laser melting of maraging steel 300. *Metals*, 9(10), 2019.

[27] D. Munro, C. Ayas, M. Langelaar, and F. Keulen. On process-step parallel computability and linear superposition of mechanical responses in additive manufacturing process simulation. *Additive Manufacturing*, 28:738–749, 2019.

[28] J. Nocedal and S. J. Wright. *Numerical optimization 2nd.* Springer, 2006.

[29] D. Pitassi, E. Savoia, V. Fontanari, A. Molinari, V. Luchin, G. Zappini, and M. Benedetti. *Finite Element Thermal Analysis of Metal Parts Additively Manufactured via Selective Laser Melting*, chapter 6. Intech, 2018.

[30] S. G. Sarvankar and S. N. Yewale. Additive manufacturing in automobile industry. *Int. J. Res. Aeronaut. Mech. Eng*, 7(4):1–10, 2019.

[31] J. Sethian and A. Wiegmann. Structural boundary design via level set and immersed interface methods. *Journal of Computational Physics*, 163(2):489–528, 2000.

[32] I. Setien, M. Chiumenti, S. van der Veen, M. San Sebastian, F. Garciandía, and A. Echeverría. Empirical methodology to determine inherent strains in additive manufacturing. *Computers & Mathematics with Applications*, 78(7):2282 – 2295, 2019.

[33] Y. Ueda, K. Fukuda, K. Nakacho, and S. Endo. A new measuring method of residual stresses with the aid of finite element method and reliability of estimated values. *Journal of the Society of Naval Architects of Japan*, 1975(138):499–507, 1975.

[34] D. Wang, Y. Yang, Z. Yi, and X. Su. Research on the fabricating quality optimization of the overhanging surface in slm process. *The International Journal of Advanced Manufacturing Technology*, 65:1471–1484, 2013.

[35] Y. Wang, J. Gao, and Z. Kang. Level set-based topology optimization with overhang constraint: Towards support-free additive manufacturing. *Computer Methods in Applied Mechanics and Engineering*, 339:591–614, 2018.

[36] M. Zhou, Y. Liu, and Z. Lin. Topology optimization of thermal conductive support structures for laser additive manufacturing. *Computer Methods in Applied Mechanics and Engineering*, 353:24–43, 2019.